AN ABSTRACT OF THE THESIS OF

Daniel Alan Peterson for the degree of Master of Science in
Mechanical Engineering presented on June 4, 2010.

Title:

Numerical Simulation of Micro/Mini-Channel based Methane-Steam Reformer

Abstract approved: _____

Sourabh V. Apte

Numerical modeling of methane-steam reforming is performed in a micro/mini-channel with heat input through catalytic channel walls. The low-Mach number, variable density Navier-Stokes equations together with multicomponent reactions are solved using a parallel numerical framework. Methane-steam reforming is modeled by three reduced-order reactions occurring on the reactor walls. The surface reactions in the presence of a catalyst are modeled as Neumann boundary conditions to the governing equations. Two catalysts are investigated: a porous Nickel substrate and a porous felt with deposited Palladium nanoparticles. The reduced-order mechanism kinetics model is coupled with the flow solver to resolve the chemical species field within the reactor geometry. The effects of the total heat input, heat flux profile, flow rate and inlet steam-methane molar concentration on production of hydrogen are investigated in detail.

The results of the parametric study give performance evaluations. An increase of hydrogen production of 10% (molar fraction) is observed when increasing the heat flux from no heat flux to a wall heat flux of 3 kW/m^2. The results from the three heat flux profiles study (constant, linear increasing, and linear decreasing) are increased hydrogen production between the linear decreasing profile (worst performer) and the linear increasing profile (best performer) of 3.5% on a molar basis. Varying flow rate from 800 ml/min to 100 ml/min results in an increase of hydrogen mole fraction of 16%. Hydrogen production is non-linearly related to the steam-methane ratio. Maximum hydrogen production is observed near a ratio of 3.0. The reaction rates may be increased by the introduction of hydrogen extraction.

Numerical Simulation of Micro/Mini-Channel based Methane-Steam Reformer

by

Daniel Alan Peterson

A THESIS

submitted to

Oregon State University

in partial fulfillment of
the requirements for the
degree of

Master of Science

Presented June 4, 2010
Commencement June 2010

Master of Science thesis of Daniel Alan Peterson presented on June 4, 2010.

APPROVED:

Major Professor, representing Mechanical Engineering

Head of the School of Mechanical, Industrial, and Manufacturing Engineering

---

Dean of the Graduate School

I understand that my thesis will become part of the permanent collection of Oregon State University libraries. My signature below authorizes release of my thesis to any reader upon request.

Daniel Alan Peterson, Author

ACKNOWLEDGEMENTS

I extend a warm thank you to all who assisted in this work especially the following. A special thanks to my advisor, Dr. Sourabh Apte, whose patient mentorship and advice has greatly enhanced my CFD problem-solving skills. My project team members Benn Eilers, Dr. Vinod Narayanan and Dr. John Schmitt, who gave support in the presence of confusing results. The Computational Flow Physics Group members Justin Finn, Andrew Cihonski and past members Ehsan Shams and Mathieu Martin. Especially, Justin who has answered countless questions and Andrew who has commiserated with me in times of puzzling results. The Thermal Fluids Sciences group at OSU. Dr. Murty Kanury for his hours of extra work teaching me combustion. I also thank the Oregon Best organization (Oregon Built Environment & Sustainable Technologies Center), which supported me financially.

And those who helped me along the way. My family, without whom I would be nothing. My parents, who have always created a loving and supportive environment. My brothers and extended family, who make going home always enjoyable. The engineering department of my *alma mater* George Fox University, whose support has been invaluable. The teachers at Central Catholic High School, who saw me through the awkward teen years. The Gardner School, where I learned to love learning. The faith communities I fellowship with, who

have blessed me. And my friends, whose support is unconditional and advice is seasoned.

TABLE OF CONTENTS

Page

1 Introduction 2

2 Literature Review 7
- 2.1 Chemical Kinetics Models . . . 8
- 2.2 Parametric Refinement . . . 10
- 2.3 Porous Catalyst Activation . . . 13
- 2.4 Additional Work . . . 14

3 Governing Equations 15
- 3.1 General Form . . . 16
- 3.2 Assumptions and Model Selection . . . 18
- 3.3 Simplified Governing Equations . . . 21

4 Chemical Kinetics 23
- 4.1 Chemical Mechanism . . . 24
- 4.2 Chemical Kinetics Modeling . . . 26
- 4.3 Numerical Implementation of Surface Reaction . . . 29

5 Verification & Validation Studies 34
- 5.1 Microchannel Flow Characteristics . . . 35
- 5.2 Flow and Heat Transfer Characteristics of a Heated Pipe . . . 38
- 5.3 Reacting Flow . . . 44
- 5.4 Chemical Kinetics Model . . . 50

6 Results 56
- 6.1 Methane-Steam Reformations . . . 59
- 6.2 Heat Flux Magnitude . . . 67
- 6.3 Flow Rate . . . 67
- 6.4 Heat Flux Profile . . . 76
- 6.5 Steam Methane Ratio . . . 79

TABLE OF CONTENTS (Continued)

Page

6.6 Experimental Facility 85

7 Summary and Conclusions 96

7.1 Conclusion 97

Appendices 100

A-1 Fluid Properties 101

A-2 Grid Refinement 104

Bibliography 106

LIST OF FIGURES

Figure Page

5.1 Velocity profiles at the center plane for different Reynolds numbers and x locations. The solid symbols (•) represent experimental data from Qu *et al.* [1], the dashed line (−−) represents numerical results from Qu *et al.* [1] and the solid line (−) represents the work presented. The velocity (U) is given in units of $[m/s]$ and the y location in $[\mu m]$. 37

5.2 Grid used to solve the constant wall temperature pipe flow validation case. 39

5.3 Velocity profiles for both the Hagen-Poiseuille parabolic profile [2] and the presented work, for a circular pipe flow. The Hagen-Poiseuille parabolic profile is shown with a dashed line (−−) and the profile from this model is shown with a solid line (−). 41

5.4 Temperature profiles for both Kakaç *et al.* [2] and the presented work are for a circular pipe with constant wall temperature. The Kakaç *et al.* [2] solution is shown with a dashed line (−−) and the profile from this model is shown with a solid line (−). 43

5.5 Schematic of the flow geometry for the reacting flow validation case. Where the reactants diffuse from right to left, react on the catalyst wall and the products diffuse from left to right. Carbon dioxide (CO_2) has a rich concentration at the catalyst (left) wall and oxegen (O_2) and carbon monoxide (CO) are in rich concnetration at the inlet (right boundary). 45

5.6 Mass fraction of carbon monoxide (CO) normalized with the CO mass fraction at the inlet, in the z (diffusion) direction expressed in units of $[m]$. The exact solution given by Mills [3] is shown by a dashed line (−−) and the work presented here is show with a solid line (−). 49

5.7 Reaction rates profiles for all three reactions considered here. For a uniform heat flux of 2 kW/m^2. The Kuznetsov model [4] predictions are shown with dashed lines (−−) and the predictions of this model are shown with solid lines (−). The three reactions are denoted. . . 52

LIST OF FIGURES (Continued)

Figure | Page

5.8 Species mole fraction profiles along the channel length for a uniform heat flux of 2 kW/m^2. Here the Kuznetsov model [4] predictions are shown with dashed lines (−−) and the predictions of this model are shown with solid lines (−). The different chemical species are denoted. 53

5.9 Reaction rates profiles for all three reactions considered here for a ramped heat flux with average magnitude of 2 kW/m^2. The Kuznetsov model [4] predictions are shown with dashed lines (−−) and the predictions of this model are shown with solid lines (−). The three reactions are denoted. 54

5.10 Species mole fraction profiles along the channel length, for a ramped heat flux with average magnitude of 2 kW/m^2. Here the Kuznetsov model [4] predictions are shown with dashed lines (−−) and the predictions of this model are shown with solid lines (−). The different chemical species are denoted. 55

6.1 Schematic of the microchannel reactor. 58

6.2 Schematic of the microchannel reactor with catalyst on the top and bottom surfaces. 59

6.3 Production of hydrogen as a molar fraction along the channel length. Here the solid lines (−) represent the presented work and the dashed lines (−−) represent the Wang *et al.* [5] predictions for three flow rates: 100 ml/min shown with downward triangles, 300 ml/min with squares and 800 ml/min with upward triangles. 62

6.4 Depletion of methane as a molar fraction along the channel length. Here the solid lines (−) represent the presented work and the dashed lines (−−) represent the Wang *et al.* [5] predictions for three flow rates: 100 ml/min shown with downward triangles, 300 ml/min with squares and 800 ml/min with upward triangles. 63

6.5 Variation of H_2 concentration along the microchannel reactor for different wall heat flux magnitudes. The flow rate is 400 ml/min; the steam-methane ratio is 2.5; and the constant wall temperature is 973 K 68

LIST OF FIGURES (Continued)

Figure | Page

6.6 Methane conversion along the microchannel reactor for different wall heat flux magnitudes. The flow rate is 400 ml/min; the steam-methane ratio is 2.5; and the constant wall temperature is 973 K . . 69

6.7 Chemical species mole fraction along the microchannel reactor for a wall heat flux magnitudes of $q'' = 3\ kW/m^2$. The flow rate is 400 ml/min; the steam-methane ratio is 2.5; and the constant wall temperature is 973 K 70

6.8 Variation of surface reaction rates for different flow rates and a steam-methane ratio of 2.5 with constant wall temperature of 973 K. 71

6.9 Variation of H_2 concentration along the microchannel reactor for different flow rates. The steam-methane ratio is 2.5; the heat flux profile is ramp up; and the constant wall temperature is 973 K . . . 72

6.10 Chemical species mole fraction along the microchannel reactor for a total flow rate of $Q_{total} = 100\ lm/min$. 74

6.11 Methane conversion along the microchannel reactor for different flow rates. 75

6.12 Variation of H_2 molar concentration along the channel wall for different heat flux profiles. The average heat flux is kept constant at 2 kW/m^2; the flow rate is 400 ml/min; and the steam-methane ratio is 2.5. 77

6.13 Variation of H_2 of wall temperature along the channel wall for different heat flux profiles. The average heat flux is kept constant at 2 kW/m^2; the flow rate is 400 ml/min; and the steam-methane ratio is 2.5. 78

6.14 Chemical species mole fraction along the microchannel reactor for a heat flux profile of ramp up and average magnitude of $q'' = 2\ kW/m^2$. 80

6.15 Methane conversion along the microchannel reactor for different heat flux profiles. 81

6.16 Variation of H_2 molar concentration along the channel wall for different steam-methane ratios. The wall temperature is kept constant at 973 K and the flow rate is 400 ml/min. 82

LIST OF FIGURES (Continued)

Figure Page

6.17 Methane conversion along the microchannel reactor for different inlet steam-methane ratio. 83

6.18 Chemical species mole fraction along the microchannel reactor for a steam-methane ratio of 3. 84

6.19 Schematic of the flow geometry of the experimental facility. 86

6.20 Grid used to model the experimental facility. 86

6.21 Pressure drop through device. The experimental pressure drop is shown with symbols and the numerical pressure drop is given with a solid line. 87

6.22 Velocity profiles of both the full geometry model and the truncated model. The full model velocity is shown with a dashed line $(--)$ and the truncated model is given with a solid line $(-)$. 89

6.23 Temperature profiles of the first four flow rates using Catalyst B, along the reactor length. 90

6.24 Contour of hydrogen molar fraction within the reactor geomentry. . 93

6.25 Contour of methane molar fraction within the reactor geomentry. . 94

6.26 Contour of velocity molar fraction within the reactor geomentry. . . 95

LIST OF TABLES

Table		Page
4.1	Hou and Hughes [6] chemical kinetics constants	28
5.1	Channel Dimensions: from the Qu *et al.* [1] geometry	36
5.2	Pressure Drop [bar] through the channel from Qu *et al.* [1]	37
5.3	Reaction characteristics from Mills [3]	48
6.1	Boundary conditions used in simulations	57
6.2	Geometry Dimensions of the three channel studied	58
6.3	Hydrogen Production Compared to Wang *et al.* [5] Results	64
6.4	Methane consumption Compared to Wang *et al.* [5] Results	65
6.5	Hydrogen Production Compared to Experimental Results for Catalyst B	91
6.6	Hydrogen Production Compared to Experimental Results for Catalyst C	92

LIST OF APPENDIX FIGURES

Figure		Page
1	Fluid dynamic viscosity of all species investigated over a temperature range of 1000 K to 1200 K.	102
2	Schematic of the microchannel reactor used for the grid refinement studies.	104
3	Velocity profiles (a) and mole fraction profiles of hydrogen (b) at a flow length of 100 mm in the cross flow direction for three grid geometries. Where Grid one has 25 CVs in the cross flow direction, Grid two has 36 CVs and grid three has 50 CVs	105

DEDICATION

To all who were told he or she would not graduate high school.

Numerical Simulation of Micro/Mini-Channel based Methane-Steam Reformer

Chapter 1 – Introduction

Finding and optimizing alternative energy sources and processes requires much investigation and innovation. Methane-steam reforming is a process by which methane (natural gas) and steam are reacted to form usable hydrogen fuel. This process produces yields of hydrogen fuel which consume 80% to 95% of the low grade methane (CH_4) provided [5]. The reactor considered here increases yields by employing the following considerations: (a) microchannel geometry (which increases the surface area and in so doing promotes fast species diffusion that accelerates the chemical reactions); (b) two catalysts where considered here (i) a porous Nickel catalyst substrate and (ii) Palladium nanoparticles deposited on a porous substrate (which allows for faster chemical reaction rates); and (c) high temperature (which also increases reaction rates) [4, 5, 7]. To achieve the high temperatures a heat flux is induced along the channel length, the source of which is solar energy. Solar energy is typically utilized in one of two ways: 1) deriving direct electrical power through photovoltaic, and 2) providing thermal energy for the endothermic chemical reactions in fuel reforming [8, 9, 10, 11]. Current photovoltaic system operate at low efficiencies, less than 5% [12, 13] for standard applications and less than 11% [14] for molecular systems. Fuel reforming is the process by which a low-grade fuel is converted into a useful fuel. Typically this process is performed to convert hydrocarbons to hydrogen fuel. Many different types of hydrocarbons are used such as butane [15, 16], iso-octane, [17, 18] or methane [4, 5, 7].

This work addresses parameter optimization for the use of solar energy in steam methane reforming. The development of a reliable numerical model allows for quick and robust design modifications. This will enable reactor design to be optimized

to increase hydrogen fuel.

Hydrogen output can be improved by the following innovations: (a) design of solar concentrators that permit energy collection at high efficiency, (b) receiver designs that will increase the chemical efficiency of an endothermic reaction for biofuel reforming, (c) process control schemes that could optimize the production of fuels and (d) operating parameters such as flow rate, steam methane ratio and heat characteristics. The technological readiness of solar concentrators is relatively high [11, 19]. Significant improvements can be made to the receiver designs, process control, and operating parameters to permit increased efficiencies with the receiver and chemical reforming.

Currently solar receivers are based most commonly on volumetric or cavity designs [20, 21, 22], wherein chemical reactions occur when the cavity constrains the reactants and products. Chemical reactions in such chambers are limited by (a) the diffusion time of the non-premixed reactants, (b) low heat transfer rates from the walls to the reactants, and (c) low volumetric absorption by the reactant gases (owing to the large volume to surface area ratio of typical designs).

The work presented here investigates an open receiver design where the receiver and the reactor are separated. The receiver walls are covered with long microchannels capable of efficient heat removal (due to increased surface area). The chemical reforming of the biomass gases will be performed inside the microchannels. This design exploits the short diffusion lengths for reactant gases in microchannels, such that the reaction may occur near stoichiometric conditions (using less excess reactant gases), thereby substantially increasing the efficiency of the system.

Such a design has several advantages: (a) reduce mixing time for non-premixed reactants owing to decreased diffusion time of the microchannels geometry, (b) high heat transfer rates in microchannels geometry, (c) eliminate absorption of solar radiation by the gas as the limiting factor for heat transfer, and (d) prevent damage to one of the microchannels causing catastrophic failure of the receiver.

In order to study the technical feasibility of such a receiver, numerical simulations were developed to study, strong endothermic reactions of methane-steam reforming within a microchannel reactor over a porous catalyst. The low-Mach number, unsteady, variable-density Navier-Stokes equations together with species mass-fraction and energy equations are solved in a microchannel. The surface chemical reactions are modeled as boundary conditions to the energy and species equations for a reduced reaction mechanism of methane-steam reforming [5, 4, 23, 6]:

$$CH_4 + H_2O \Longleftrightarrow CO + 3H_2; \qquad \Delta H^0_{298} = +206\ kJ/mol, \tag{1.1}$$

$$CO + H_2O \Longleftrightarrow CO_2 + H_2; \qquad \Delta H^0_{298} = -41\ kJ/mol, \tag{1.2}$$

$$CH_4 + 2H_2O \Longleftrightarrow CO_2 + 4H_2; \qquad \Delta H^0_{298} = +167\ kJ/mol. \tag{1.3}$$

There have been several studies on micro/minichannel reactors with Rhodium, Palladium or Nickel catalysts arranged in the form of a packed bed [23, 6, 7, 24]. Recently, Wang *et. al.* [5] investigated the effects of steam-methane inlet ratios

and flow rates on hydrogen production in planar solid-oxide fuel cells (SOFC) using experimental and numerical modeling at steady-state. Kuznetsov & Kozlov [4] investigated the effect of heat flux distribution on methane-steam reforming using reduced reaction mechanisms in a microchannel with Nickel catalyst. The goal of this work is to investigate the effect of inlet steam-methane ratio, the distribution and amount of external heat flux provided and the flow rate on the production of hydrogen. Accordingly, the parameters varied in this work are the heat flux magnitude ($|\dot{q}''|$), heat flux profile ($\dot{q}'' = f(x)$), steam-methane ratio ($S : M$) and total flow rate ($\dot{Q}$).

Chapter 2 – Literature Review

This section presents two chemical kinetics models and a brief overview of the experimental tests from which these models are derived. The correct numerical model coupled with the physically accurate chemical kinetics model is critical to correctly simulate chemical species concentration fields. A method used to characterize the porous catalyst will also briefly be considered.

Investigations of methane-steam reformation typically produce one of two results, either a chemical kinetics model (or model refinement) or geometry and operating parameters optimization. The chemical kinetics model characterizes the chemical reaction rates. (These rates are typically assumed negligible in the gas phase and are found only at the catalyst surface [7, 23, 25]). The kinetics model is used to simulate the species mass fraction and thermal boundary conditions for application in numerical simulations. The parametric studies result in optimal reactor designs and operating conditions. Parametric studies investigate physical conditions such as heat flux magnitude, heat flux profile, steam-methane ratio and flow rate.

2.1 Chemical Kinetics Models

There are two methods for resolving the chemical kinetics. First, a model introduced by Xu and Froment [23], which relates the reaction rates to the partial pressures of both the reactants and products, the reaction rate constant (k), and reaction equilibrium constants (K). This model is highly dependent on the experimentally-found kinetics constants. Hou and Hughes' model [6] (based on the

Xu model) 11 introduces experimental constants . This model is the most commonly used for methane-steam reforming, as in the work done by [6, 5, 4, 23]. This model will be referred to as the experimental chemical kinetics model. Owing to the high degree of sensitivity this model has to the experimentally found constants. The chemical reaction equations are expressed below (from Hou *et al.*. [6]):

$$r_1 = \frac{k_1 \left(\frac{P_{CH_4} P_{H_2O}^{0.5}}{P_{H_2}^{1.25}} \right) \left(1 - \frac{P_{CO} P_{H_2}^3}{K_{p1} P_{CH_4} P_{H_2O}} \right)}{\left(1 + K_{CO} P_{CO} + K_{H_2} P_{H_2}^{0.5} + K_{H_2O} \left(P_{H_2O} / P_{H_2} \right) \right)^2}, \tag{2.1}$$

$$r_2 = \frac{k_2 \left(\frac{P_{CO} P_{H_2O}^{0.5}}{P_{H_2}^{0.5}} \right) \left(1 - \frac{P_{CO_2} P_{H_2}}{K_{p2} P_{CO} P_{H_2O}} \right)}{\left(1 + K_{CO} P_{CO} + K_{H_2} P_{H_2}^{0.5} + K_{H_2O} \left(P_{H_2O} / P_{H_2} \right) \right)^2}, \tag{2.2}$$

$$r_3 = \frac{k_3 \left(\frac{P_{CH_4} P_{H_2O}}{P_{H_2}^{1.75}} \right) \left(1 - \frac{P_{CO_2} P_{H_2}^4}{K_{p3} P_{CH_4} P_{H_2O}^2} \right)}{\left(1 + K_{CO} P_{CO} + K_{H_2} P_{H_2}^{0.5} + K_{H_2O} \left(P_{H_2O} / P_{H_2} \right) \right)^2}. \tag{2.3}$$

The second method takes the model from analytically-based equations presented by Kenneth, Turns and Versteeg [26, 27, 28]. This model is also employed to simulate methane reformation by Deutschmann *et al.* and Appel *et al.* [7, 24]. (Deutschmann used oxygen not steam as the oxidizer and Appel used a Rhodium catalyst. This model relates reaction rates to reactants' concentrations and the experimentally-found reaction rate constants (k). This second model [7, 24] gives results comparable to those predicted by the first model [6, 5, 4, 23] and is computationally less expensive . The chemical reaction equations are expressed below:

$$r_1 = k_1 \left(\frac{\rho}{\mathcal{M}_{CH_4}}\right)\left(\frac{\rho}{\mathcal{M}_{H_2O}}\right) Y_{CH_4} Y_{H_2O}, \tag{2.4}$$

$$r_2 = k_2 \left(\frac{\rho}{\mathcal{M}_{CO}}\right)\left(\frac{\rho}{\mathcal{M}_{H_2O}}\right) Y_{CO} Y_{H_2O}, \tag{2.5}$$

$$r_3 = k_3 \left(\frac{\rho}{\mathcal{M}_{CH_4}}\right)\left(\frac{\rho}{\mathcal{M}_{H_2O}}\right)^2 Y_{CH_4} Y_{H_2O}^2. \tag{2.6}$$

The reaction rates given here correspond with the three reactions studied:

$$CH_4 + 2H_2O \rightarrow CO_2 + 4H_2; \qquad \Delta H^0_{298} = +167\ kJ/mol, \tag{2.7}$$

$$CO + H_2O \rightarrow CO_2 + H_2; \qquad \Delta H^0_{298} = -41\ kJ/mol, \tag{2.8}$$

$$CH_4 + H_2O \rightarrow CO + 3H_2; \qquad \Delta H^0_{298} = +206\ kJ/mol. \tag{2.9}$$

2.2 Parametric Refinement

Parameter studies where not performed by Xu and Froment [23] or by Hou and Hughes [6]. Instead their investigations focused on introducing a methane-steam reforming chemical kinetics model and refining the model experimentally.

Kuznetsov & Kozlov [4] investigated two heat flux profiles and the effects of heat flux magnitude on hydrogen production. Two channels were studied, one with height 0.5 mm and length 0.1125 m and a second with height 1.2 mm and

length 0.27 m. Both channels collapse into a characteristic channel with scaled length of 225, where length is scaled by height (L/h). Both channels have an entry length without catalyst. In both cases the scaled length of this catalyst section is 30 height lengths. The heat flux is applied only to the catalyst section (leaving the entry length unheated).

Both uniform and nonuniform heat flux profiles are considered in the numerical work shown here and by Kuznetsov *et al.* [4] . Uniform heat flux enforces a constant heat flux along the catalyst length. The nonuniform (ramp) heat flux varies the heat flux linearly along the channel length with a maximum at the exit. To evaluate the effects of heat flux profile on the chemical kinetics, each heat flux was tested for the same mean heat flux magnitude. Kuznetsov & Kozlov [4]concluds for the specified geometry the nonuniform heat flux mostly heats the exit gases, which is wasted heat and unnecessary to the reaction.

The heat flux magnitudes considered in this study are 0, 1, 2, 2.5 and 3 kW/m^2. To compare the effects of heat flux, species concentration profiles were generated for each heat flux magnitude. Also the methane conversion fraction for each heat flux magnitude was calculated and compared. The following expected methane conversion and heat flux correlation were observed: the methane conversion of the zero heat flux condition was nearly 20% and grows asymptotically close to 100% with increasing heat flux.

Wang *et al.* [5] investigated the effects of steam methane inlet ratio, flow rates, operation pressure and wall temperature. The species concentrations through the flow length were used to compare the effects of these parameters on hydrogen

production. Wang *et al.* [5] studied a channel of height 4.5 mm and total length of 0.13 m, with a catalyst section of 0.1 m centered in the channel length. This channel geometry gives a scaled length (L/h) of approximately 29 and an entry scaled length of 3.33.

To relate these parameters to reaction efficiency Wang *et al.* [5] compared the methane conversion fraction for varying test parameters. The methane conversion fraction tended to increase with decreasing steam carbon ratio until the ratio reached approximately 2.5. Then the hydrogen production decreased with the decreasing steam methane ratio. The methane conversion is less sensitive to steam methane ratio than other parametric changes. Methane conversion varies an order of magnitude more with variations in flow rate, wall temperature, and, in some cases, operating pressure.

The effects of flow rate were also studied by comparing the methane conversion fraction. A expected trend correlating increasing methane conversion with decreased flow rate was observed. Approximately one half of the methane was converted at the highest flow rate (320 ml/min of methane at the inlet) and nearly 90% at the slowest flow rate (40ml/min of methane at the inlet). Methane conversion may not be a useful measure when increased hydrogen output is the aim. Therefore, the product of the hydrogen molar fraction and the flow rate may present a better parameter to measure success. Wang *et al.* [5] also considered the effect of pressure and temperature on hydrogen production. Methane conversion fraction increases with increased reactor wall temperature and operating pressure.

2.3 Porous Catalyst Activation

The chemical kinetics are highly dependent on the catalyst surface, therefore the catalyst surface must be characterized. The high degree of uncertainty in characterizing the porous substrates introduces complex modeling issues which must be resolved. Wang *et al.* [5] introduces a porous activation factor by which these porous uncertainties can be addressed. This method requires running numerical and experiential tests in parallel then comparing the concentrations for both experimental and numerical results. These calculations produce the porous activation factor which is introduced to scale the reaction rates to experimentally found levels. This method results in the reaction rates in the work by Wang *et al.* [5]take the following form:

$$r_1 = C_a \frac{k_1 \left(\frac{P_{CH_4} P_{H_2O}}{P_{H_2}^{1.75}}\right)\left(1 - \frac{P_{CO_2} P_{H_2}^4}{K_{p1} P_{CH_4} P_{H_2O}^2}\right)}{\left(1 + K_{CO} P_{CO} + K_{H_2} P_{H_2}^{0.5} + K_{H_2O}\left(P_{H_2O}/P_{H_2}\right)\right)^2}, \tag{2.10}$$

$$r_1 = C_a \frac{k_1 \left(\frac{P_{CH_4} P_{H_2O}^{0.5}}{P_{H_2}^{1.25}}\right)\left(1 - \frac{P_{CO} P_{H_2}^3}{K_{p1} P_{CH_4} P_{H_2O}}\right)}{\left(1 + K_{CO} P_{CO} + K_{H_2} P_{H_2}^{0.5} + K_{H_2O}\left(P_{H_2O}/P_{H_2}\right)\right)^2}, \tag{2.11}$$

$$r_3 = C_a \frac{k_3 \left(\frac{P_{CO} P_{H_2O}^{0.5}}{P_{H_2}^{0.5}}\right)\left(1 - \frac{P_{CO_2} P_{H_2}}{K_{p3} P_{CO} P_{H_2O}}\right)}{\left(1 + K_{CO} P_{CO} + K_{H_2} P_{H_2}^{0.5} + K_{H_2O}\left(P_{H_2O}/P_{H_2}\right)\right)^2}, \tag{2.12}$$

Whereas in this work, they take the form shown below:

$$r_1 = C_a k_1 \left(\frac{\rho}{\mathcal{M}_{CH_4}}\right)\left(\frac{\rho}{\mathcal{M}_{H_2O}}\right) Y_{CH_4} Y_{H_2O}, \tag{2.13}$$

$$r_2 = C_a k_2 \left(\frac{\rho}{\mathcal{M}_{CO}}\right)\left(\frac{\rho}{\mathcal{M}_{H_2O}}\right) Y_{CO} Y_{H_2O}, \tag{2.14}$$

$$r_3 = C_a k_3 \left(\frac{\rho}{\mathcal{M}_{CH_4}}\right)\left(\frac{\rho}{\mathcal{M}_{H_2O}}\right)^2 Y_{CH_4} Y_{H_2O}^2, \tag{2.15}$$

where, C_a represents the porous catalyst activation factor. This porous activation catalyst factor is then varied until the bulk mean hydrogen molar species fraction compares well with those found experimentally. Employing this method Wang *et al.* [5] achieved results consistent with those found experimentally.

2.4 Additional Work

In this work, all the above mentioned parameters and one additional heat flux profiles were considered in tandem, using the analytically based chemical kinetics model. The kinetics model was adapted to include the three chief chemical reactions (Equations 1.1, 1.2 and 1.3), which Xu *et al.* [23] found to be the primary reactions from the 11 reactions found in the study of methane steam reformation. This study applied the geometry studied by Wang *et al.* [5]. The parameters studied here are heat flux magnitude ($|\dot{q}''|$), heat flux profile ($\dot{q}'' = f(x)$), steam methane ratio ($S : M$) and flow rate ($\dot{Q}$).

Chapter 3 – Governing Equations

Computational fluid dynamics is the parallel solving of the equations governing the interaction of flow characteristics, including velocity, pressure, temperature and species concentrations. Solving these governing equations gives two or three dimensional characteristic fields of the aforementioned flow properties. This chapter will detail these governing equations, as well as the assumptions and closure models used to simplify the equations and conclude with reduced governing equations.

3.1 General Form

The low-Mach number, unsteady, variable-density Navier-Stokes equations (equation 3.2) together with species mass-fraction and energy equations are solved in a microchannel. These equations govern the conservation of mass, momentum, energy and chemical species. In this work, these governing equations were referenced from [4, 29, 30].

Mass:

$$\frac{\partial \rho}{\partial t} + \frac{\partial}{\partial x_j}(\rho u_j) = 0 \tag{3.1}$$

Momentum:

$$\frac{\partial (\rho u_i)}{\partial t} + \frac{\partial}{\partial x_j}(\rho u_i u_j) = -\frac{\partial p}{\partial x_i} + \frac{\partial \tau_{ij}}{\partial x_j} \tag{3.2}$$

Energy:

$$\frac{\partial (\rho h)}{\partial t} + \frac{\partial}{\partial x_j}(\rho u_j h) = -\frac{\partial q_j}{\partial x_j} + \mu \Phi_v + \frac{dp}{dt} \tag{3.3}$$

Species:

$$\frac{\partial(\rho Y_i)}{\partial t} + \frac{\partial}{\partial x_j}(\rho u_j Y_i) = \frac{\partial}{\partial x_j}\left(\rho \mathcal{D}_{i,m} \frac{\partial Y_i}{\partial x_j}\right) + \dot{\omega}_i'''; \text{ i} = 1...\text{N}_\text{s} \tag{3.4}$$

and τ is the modeled viscous stress seen in equation 3.5,

$$\tau = \mu\left(\frac{\partial}{\partial x_j}(u_j) + \left(\frac{\partial}{\partial x_j}(u_j)\right)^T\right), \tag{3.5}$$

and Φ is the viscous heating as seen in equation 3.6,

$$\begin{aligned}
\Phi_v &= 2\mu\left(\left(\frac{\partial u}{\partial x}\right)^2 + \left(\frac{\partial v}{\partial y}\right)^2 + \left(\frac{\partial w}{\partial z}\right)^2\right) \\
&+ 2\mu\left(\frac{1}{2}\left(\frac{\partial v}{\partial x} + \frac{\partial u}{\partial y}\right)^2 + \frac{1}{2}\left(\frac{\partial w}{\partial y} + \frac{\partial v}{\partial z}\right)^2 + \frac{1}{2}\left(\frac{\partial u}{\partial z} + \frac{\partial w}{\partial x}\right)^2\right) \\
&- 2\mu\left(\frac{1}{3}\left(\frac{\partial u}{\partial x} + \frac{\partial v}{\partial y} + \frac{\partial w}{\partial z}\right)^2\right).
\end{aligned} \tag{3.6}$$

Where N_s, ρ_v, u_i, Y_i, p, h, q_j, and Φ_v represent the number of species transport equations, density, velocity components, species mass fraction, pressure, total enthalpy, heat flux due to conduction and viscous dissipation, respectively. The mixture is assumed as an ideal gas. Viscosity, thermal conductivity, and the binary diffusion coefficient ($\mathcal{D}_{i,m}$) depend upon the local species composition and temperature.

3.2 Assumptions and Model Selection

This section will discuss ten assumptions made in this work for purposes of simplifying the governing equations. Justification for these assumptions will be given and the simulation implementation will be addressed.

In this work the following are assumed negligible; (1) viscous heating, (2) gradients in thermodynamic pressure, (3) bulk viscosity, (4) body forces, (5) pressure driven diffusion and (6) thermal radiation. The following assumptions are also made; (7) low mach number, (8) constant specific heat, (9) ideal gas and (10) no gaseous reactions.

Viscous heating is orders of magnitude smaller than the input heat flux, therefore it is assumed to be negligible (assumption 1). This causes the Φ_v term (see equation 3.6) to go to zero and drops from equation 3.2. The thermodynamic pressure is assumed to be constant and set to the value of p_0 (assumption 2). This allows the fluid properties to be found for constant pressure. In assuming no bulk viscosity (assumption 3), the viscous stress model is simplified, as seen in equation 3.5. This work assumes the effect of gravity to be negligible along with any other body forces (assumption 4), such as buoyancy. The body force term, $\mathbf{f}$, drops from equation 3.2. Assuming no pressure driven diffusion forces all diffusion to be concentration driven (assumption 5). The heat transfer in this work is limited to convection and conduction. Therefore the heat transfer from thermal radiation is taken to be insignificant (assumption 6). Modeling with a low mach number allows for the neglecting of pressure effects on the properties [30]. Assuming the

specific heat to be constant (Assumption 8) simplifies the expression for enthalpy (see equation 3.9). Therefore the variation in specific heat at typical operating temperatures is less than 1.44% (at $\dot{q} = 2.5kw/m^2$). This model assumes the gas to be ideal, this allows the Ideal Gas law to be used (assumption 9). It has been shown that the reaction rates in the gaseous phase are orders of magnitude slower than those at the catalyst wall [7]. Therefore, this work removes the chemical species source term from the bulk flow which allows the reaction to become a boundary condition at the catalyst wall (assumption 10).

Applying these assumptions to the governing equations produce the following changes. Equation 3.1 (conservation of mass) remains unchanged. In equation 3.2 (conservation of momentum) the only term which is removed is the body force term. However, the viscous model term is changed according to the assumption made. Both equations allow density to very. with temperature and chemical species, which is expressed in equation 3.7. This relationship uses the Ideal Gas Law, which assumption 2 allows. Density is expressed in terms of known properties.

$$\rho = \frac{p_0 M_{mix}}{TR} \tag{3.7}$$

Where, R is the universal gas constant, T is the temperature in K and M_{mix} is molecular weight of the mixture, given in equation 3.8, where N_s is the total number of species.

$$M_{mix} = \frac{1}{\sum_i^{N_s} \frac{Y_i}{M_i}} \tag{3.8}$$

The energy equation is written in terms of enthalpy. Owing to the assumption of constant thermodynamic pressure (or low mach number), the enthalpy is not pressure dependent. Heat generation at the wall creates heat flux term in the gas phase, which includes conduction and convection heat transfer terms.

The temperature field is solved by converting the enthalpy field to temperature. The relationship between enthalpy (h) and local temperature (T) is considered in the following equation:

$$h = h^o_{f_{mix}} + \int_{T_{C_{p,ref}}}^{T} c_{p_{mix}} dT, \tag{3.9}$$

where,

$$h^o_{f_{mix}} = \sum_{i}^{N} Y_i h^o_{f_i}. \tag{3.10}$$

Where, h is the specific enthalpy of the mixture, $h^o_{f_{mix}}$ is the enthalpy of formation of the mixture, $h^o_{f_i}$ is the enthalpy of formation for the i^{th} species, $c_{p_{mix}}$ is the specific heat of the mixture (the mass weighted average of the species' specific heat), N_s is the total number of species and $T_{C_{p,ref}}$ is a reference temperature.

As per the ten operating assumptions described above, the specific heat can be taken outside of the integration. Simplifying the integration (as seen in equation 3.11) and combining with equation 3.10, gives equation 3.12.

$$h = h^o_{f_{mix}} + c_{p_{mix}} \left(T - T_{C_{p,ref}} \right) \tag{3.11}$$

$$h = \sum_{i}^{N} Y_i h_{f_i}^{o} + c_{p_{mix}} \left(T - T_{C_{p,ref}} \right) \tag{3.12}$$

The local value of the enthalpy is found, then converted to temperature, by using the following expression:

$$T = \frac{h - \sum_{i}^{N} Y_i h_{f_i}^{o}}{c_{p_{mix}}} + T_{C_{p,ref}}. \tag{3.13}$$

The reaction rates in the gaseous phase are orders of magnitude slower than those at the catalyst wall (no homogeneous reactions) [7]. This allows the chemical kinetics at the catalyst wall to be collapsed into a boundary condition. Therefore, the gaseous chemical species source term will drop from equation 3.4. All these equations are written in terms of species mass fraction, (Y_i) but can be converted easily into molar fraction (X_i) as shown in equation 3.14 below.

$$X_i = \frac{\frac{Y_i}{M_i}}{\sum_{j}^{N_s} \left(\frac{Y_j}{M_j} \right)} \tag{3.14}$$

3.3 Simplified Governing Equations

The ten assumptions were applied to the governing equations 3.1 through 3.4. The simplified equations are collected here:

Mass:

$$\frac{\partial \rho}{\partial t} + \frac{\partial}{\partial x_j}(\rho u_j) = 0 \tag{3.15}$$

Momentum:

$$\frac{\partial(\rho u_i)}{\partial t} + \frac{\partial}{\partial x_j}(\rho u_i u_j) = -\frac{\partial p}{\partial x_i} + \frac{\partial}{\partial x_j}\left(\mu \frac{\partial}{\partial x_j}(u_j)\right) \tag{3.16}$$

Energy:

$$\frac{\partial(\rho h)}{\partial t} + \frac{\partial}{\partial x_j}(\rho u_j h) = -\frac{\partial q_j}{\partial x_j} \tag{3.17}$$

Species:

$$\frac{\partial(\rho Y_i)}{\partial t} + \frac{\partial}{\partial x_j}(\rho u_j Y_i) = \frac{\partial}{\partial x_j}\left(\rho \mathcal{D}_{i,m} \frac{\partial Y_i}{\partial x_j}\right);\ \mathrm{i} = 1...\mathrm{N_s} \tag{3.18}$$

Both the fluid properties and the chemical kinetics need to be determined from experimental data. This work used [31] for μ and c_p as functions of temperature; M_i and $h^0_{f_i}$ as taken from [32]. The diffusion coefficients $\mathcal{D}_i$ is taken from [4] and the chemical kinetics (which will be investigated in subsequent chapters) were taken from [6, 5, 4, 7, 23, 24].

Chapter 4 – Chemical Kinetics

4.1 Chemical Mechanism

Complex chemical kinetics govern the generation and depletion of chemical species in the reacting flow. Accurate modeling of the kinetics is vital for correctly predicting the chemical concentrations within the reactor channel. This chapter investigates two subjects: first, the general chemical kinetics derived empirically and second, the particular experimentally-derived kinetics governing methane steam reformation over a catalyst.

The global reaction rates governing the production and depletion of the chemical species are a function of the multiple steps within a complex kinetics. Xu and Froment [23] published an eleven-step mechanism for this methane-steam reforming given below:

$$H_2O + CO \rightarrow H_2 + CO_2 \tag{4.1}$$

$$CH_4 + H_2O \rightarrow 3H_2 + CO \tag{4.2}$$

$$CH_4 + 2H_2O \rightarrow 4H_2 + CO_2 \tag{4.3}$$

$$CH_4 + CO_2 \rightarrow 2H_2 + 2CO \tag{4.4}$$

$$CH_4 + 3CO_2 \rightarrow 2H_2O + 4CO \tag{4.5}$$

$$CH_4 \rightarrow 2H_2 + C \tag{4.6}$$

$$2CO \rightarrow C + CO_2 \tag{4.7}$$

$$H_2 + CO \rightarrow H_2O + C \tag{4.8}$$

$$2H_2 + CO_2 \rightarrow 2H_2O + C \tag{4.9}$$

$$CH_4 + 2CO \rightarrow 2H_2O + 3C \tag{4.10}$$

$$CH_4 + CO_2 \rightarrow 2H_2O + 2C \tag{4.11}$$

Xu *et al.* [23] found only the first three reactions were significant in the modeling of this reaction (reaction one (4.1), reaction two (4.2) and reaction three (4.3)). The experiments by [23, 6] found no carbon buildup on the catalyst surface dismissing all equations with solid carbon as a product. The small production of carbon dioxide (CO_2) allows for the dismissal of the reactions with carbon dioxide as a reactant, which agrees with the analysis of [23, 6].

$$CH_4 + H_2O \rightarrow 3H_2 + CO$$

$$H_2O + CO \rightarrow H_2 + CO_2$$

$$CH_4 + 2H_2O \rightarrow 4H_2 + CO_2$$

At the atomic level, these reactions can be modeled as molecular collisions. This work investigates reactions only on the catalyst wall. Therefore molecular collisions are rather forced reactions on the catalyst openings (uncovered catalyst sites) which are governed by the seven steps in the classic catalyst model described by Froment [33]; (1) diffusion of reactants to the catalyst, (2) transport into catalyst pore by

reactants, (3) absorption of reactants on to a catalytic site, (4) surface reaction of reactants, (5) desorption of products from the catalyst site, (6) transport of products through catalyst pores and (7) diffusion from the catalyst surface into the bulk flow. This work assumes the absorption and desorption time lengths do not limit the rate of reaction.

4.2 Chemical Kinetics Modeling

To introduce the chemical kinetics model consider a simple bimolecular collision reaction, as presented by Turns [27]. This model will develop a reaction rate of a simple model, where two species collide and react as expressed in the following equation 4.12.

$$\nu'_a A + \nu'_b B \rightarrow \nu''_c C + \nu''_d D \tag{4.12}$$

The reaction rate is expressed in terms of the rate coefficient (k) and the concentration of the reactants [N], as seen in equation 4.13. This reaction rate gives an expression of the speed of the reaction, which is utilized in finding creation or depletion rates for each chemical species. This reaction coefficient is a function of multiple variables including activation energy, temperature and an experimentally found pre-exponential and will be discussed further below.

$$r_k = \frac{d[A]}{dt} = -k_k [A]^{\nu'_a} [B]^{\nu'_b}, \tag{4.13}$$

where r is the reaction rate, square brackets $[n]$ indicate molar concentration of the n^{th} species and k is the rate coefficient. The negative sign denotes that species A is being consumed in this reaction.

This reaction rate is dependent on local concentrations as well as temperature; each step in the kinetic model has a corresponding local reaction rate. The reaction rates used in this work will be described in detail after the foundational kinetic models are described.

To calculate the reaction rate of this simple reaction 4.12, first the rate coefficient must be calculated. Full models expressing this rate coefficient derived from first principles do exist but will not be discussed. For this work the Arrhenius model will be used which is expressed in simple form in equation 4.14. This is an empirically-driven, experimentally-refined model.

$$k_k = A_k T^{\alpha} exp\left(-\frac{E_{a,k}}{RT}\right), \tag{4.14}$$

where; A_i is the experimentally found pre-exponential constant of the i^{th} species; α is an exerimentally found temperature dependence term (which has been found to be zero by [6, 23]); E_a is the activation energy for this reaction with units of $[kJ/kmol]$; R is the universal gas constant with units of $[kJ - K/kmol]$ and T is the temperature in $[K]$.

The rate coefficient (k) must be refined experimentally. Experiments were carried out until nearly steady-state solutions were achieved. The model predictions were compared to the experimental results and analyzed using a non-linear

least-squares calculation. Based on these results, the model was refined by the investigators (Hou and Hughes [6]) who iteratively changed the reaction rate models. These models are considered accurate when the numerical results matched experimental findings (i.e. if the rate coefficient, k, was found to be negative the model was rejected).

Table, 4.1 gives the experimentally-found constants allowing closure in the chemical kinetics model.

Table 4.1: Hou and Hughes [6] chemical kinetics constants

Experimental coefficient	Value	Units
$E_{a,1}$	209.2	kJ/mol
$E_{a,2}$	15.4	kJ/mol
$E_{a,3}$	109.4	kJ/mol
A_1	5.922×10^8	
A_2	6.028×10^{-4}	
A_3	1.093×10^3	

In the microchannel-based solar reactor, chemical reactions can occur in the gaseous phase as well as a series of reactions on the catalyst surface. Past studies by Deutschmann & Schmidt [7] on oxidation of steam in a tubular model showed that for atmospheric pressures, the gas-phase reactions contributed negligibly to the oxidation process. However, increases in reactor pressure beyond 10 bar resulted in sensitivity of the oxidation process to the gas-phase reactions. In the present work, the numerical experiments were performed at atmospheric conditions while ignoring the gas-phase reactions. The numerical solver presented in this work is, however, capable of accounting for the gaseous-phase chemical kinetics.

In this work the reactions are limited to the catalyst surface. This allows the

chemical kinetics and reaction rates to collapse into a boundary condition. To implement this boundary condition a coupled model must be developed. This model will express the creation and depletion rates of each chemical species as a function of the corresponding reaction rates. This model will be used as a boundary condition for solving the governing equation 3.4. A similar model must be developed as a boundary condition for the energy governing equation. This method is also seen in the work of Kuznetsov *et al.* [4].

The catalytic reaction rates are nonlinear relations comprising the reactant species concentrations and the local temperature. Modeling of detailed chemical kinetics pathways for catalytic reactions on the surface have been performed [7, 34]. However, calculations can become prohibitively expensive for time-resolved simulations performed in the present work. A reduced reaction mechanism with the following two endothermic (equations 1.1,1.3) and one exothermic water-gas shift (equation 1.2) global reactions was used to model the chemical conversion.

4.3 Numerical Implementation of Surface Reaction

To calculate the reaction rates, the classical kinetic model was employed, wherein the reaction rates for each chemical reactions can be formulated as follows: [26, 27],

$$r_k = k_k \Pi_{i=1}^{N_s} \left[\mathrm{C}_i\right]^{\nu'_{ki}}, \tag{4.15}$$

$$k_k = A_k \exp\left(-\frac{E_{a,k}}{RT}\right), \tag{4.16}$$

where C_i denotes the concentration of the i^{th} chemical species in the mixture $[mol_i/m^3]$, k_k is the specific reaction rate constant for the k^{th} reaction and ν'_{ki} which is dimensionless, is the stoichiometric coefficient of the i^{th} chemical species in the k^{th} reaction. The reaction activation energy ($E_{a,k}$), the activation constants A_k and α_k for each k^{th} reaction are obtained from experimental data, as seen in Table 4.1 [6, 23]. Predictive capability of the numerical approach depends on accurate characterization of the surface reactions rates. Detailed chemical kinetics pathways for catalytic surface reactions [7, 34] were used in the modeling of the catalytic reaction on the channel surface. In the present work, a reduced reaction mechanism is used to reduce the computational cost. Previous studies on methane-steam reforming by Wang *et al.* [5] and Kutnetsov *et al.* [4] use similar three-step reduced reaction mechanisms.

After solving the surface reaction rates, the catalytic conversion is then modeled simply through the following boundary conditions for the species mass-fractions and temperature equations [4, 7] (which will be further discussed in this section):

$$-\rho \mathcal{D}_i \frac{\partial Y_i}{\partial n} = \dot{s}_i \mathcal{M}_i, \tag{4.17}$$

$$-k\frac{\partial T}{\partial n} = \sum_k r_k \Delta H_{R,k} + q''_{wall}, \tag{4.18}$$

where $\dot{s}_i$ is the rate of chemical species adsorption or desorption at the catalyst surface; $\mathcal{M}_i$ is the molecular weight of species i, q_{wall}; is the rate of external heat supplied to the wall; $\Delta H_{R,k}$ is the heat of reaction; and r_k is the reaction rate

of the k^{th} surface reaction. The surface adsorption and desorption rates depend on the coverage of the catalyst over the surface and surface site density [4, 7, 24]. In the present work, uniform catalyst surface density is assumed for the reactor conditions.

The quality of the catalyst surface changes over time during methane-steam reforming. A simpler approach is to assume uniform catalyst surface density and calibrate the reaction rates through detailed validation studies for specific heat distributions and reactor conditions.

Here, r_1, r_2, and r_3 refer to the above system of reactions (4.1, 4.2 and 4.3):

$$r_1 = k_1 \left(\frac{\rho}{\mathcal{M}_{CH_4}}\right)\left(\frac{\rho}{\mathcal{M}_{H_2O}}\right) Y_{CH_4} Y_{H_2O}, \tag{4.19}$$

$$r_2 = k_2 \left(\frac{\rho}{\mathcal{M}_{CO}}\right)\left(\frac{\rho}{\mathcal{M}_{H_2O}}\right) Y_{CO} Y_{H_2O}, \tag{4.20}$$

$$r_3 = k_3 \left(\frac{\rho}{\mathcal{M}_{CH_4}}\right)\left(\frac{\rho}{\mathcal{M}_{H_2O}}\right)^2 Y_{CH_4} Y_{H_2O}^2. \tag{4.21}$$

These reaction rates must be converted into molar species adsorption and desorption rates. Which is a summation over all reactions on the catalyst surface scaled by the stoichiometric coefficient of the chemical species under investigation. When the species are being consumed the coefficient becomes negative. The surface adsorption/desorption rates for each i^{th} species are obtained as:

$$\dot{s}_i = \sum_{k=1}^{N_r=3} \left(r_k(\nu''_{ki} - \nu'_{ki}) \right). \tag{4.22}$$

Which is applied to the reactions studied here:

$$\dot{s}_{CH_4} = r_1(0-1) + r_2(0-0) + r_3(0-1), \tag{4.23}$$

$$\dot{\mathrm{s}}_{\mathrm{H_2O}} = \mathrm{r}_1(0-1) + \mathrm{r}_2(0-1) + \mathrm{r}_3(0-2), \tag{4.24}$$

$$\dot{\mathrm{s}}_{\mathrm{H_2}} = \mathrm{r}_1(3-0) + \mathrm{r}_2(1-0) + \mathrm{r}_3(4-0), \tag{4.25}$$

$$\dot{\mathrm{s}}_{\mathrm{CO}} = \mathrm{r}_1(1-0) + \mathrm{r}_2(0-1) + \mathrm{r}_3(0-0), \tag{4.26}$$

$$\dot{\mathrm{s}}_{\mathrm{CO_2}} = \mathrm{r}_1(0-0) + \mathrm{r}_2(1-0) + \mathrm{r}_3(1-0). \tag{4.27}$$

In this work, chemical species concentration gradients (in the cross flow direction) will be specified as a boundary condition. This concentration flux is the function of the creation and depletion model. The appearance and disappearance of chemical species is handled as a source or sink term and is expressed for each species. This source/sink term is described as a summation over all reactions of the product of the reaction rate and the stoichiometric molar fraction of the i^{th} chemical species as seen in equation 4.22.

Performing a mass balance, one recovers an expression equating the net species mass fraction converted at the catalyst surface to the mass diffusion into the bulk flow, as seen in equation 4.28. This expression allows one to write the boundary condition in terms of known properties ρ, α_i and M_i and the closure model developed for the source/sink term.

$$-\rho\alpha_i \frac{\partial Y_i}{\partial y} = s_i M_i \tag{4.28}$$

Similarly, the endothermic and exothermic natures of these reactions require an additional boundary condition for the energy equation. This boundary condition will be given as the thermal flux, in the cross flow direction. The net energy required, or delivered by a reaction, is expressed as a summation over all reactions of the product of the enthalpy of reactions and the reaction rates. This model is seen in equation 4.29.

$$q''_k = \sum_{k=1}^{3} (r_k \Delta H_k) \tag{4.29}$$

To incorporate this reaction heat flux into the boundary condition of the energy equation, an energy balance must be performed at the catalyst wall. This balance gives an expression including thermal conduction, heat of reaction, and heat input at the wall as seen in equation 4.30.

$$-k \frac{\partial T}{\partial n} = \sum_k r_k \Delta H_{R,k} + q''_{wall} \tag{4.30}$$

These chemical kinetic models were coupled with the fluid model and solved simultaneously to give the results presented in this work.

Chapter 5 – Verification & Validation Studies

The numerical model and solver is first verified and validated for a number of test cases: (i) velocity field within a microchannel flow, (ii) thermal and velocity field within a pipe flow, (iii)reaction rates along reactor length of methane-steam reform (chemical kinetics), (iv) chemical species mass fraction fields within a methane-steam reactor and (v) the pressure, velocity and mass species fields within an experimental reactor studied in parallel with this model. These validation cases show good agreement between the expected results and those predicted by the model considered in this study.

5.1 Microchannel Flow Characteristics

To solve for the correct species mass fraction field, first the velocity field must be solved. To validate that the work presented here is correct, the results from Martin *et al.* [35] and Qu *et al.* [1] where replicated for flow in a microchannel. Here the pressure drop and velocity profile within a microchannel where found numerically and compared to known experimental and numerical results from Qu *et al.* [1]. In this study, a three-dimensional microchannel was investigated at varying Reynolds numbers ($Re_{ch} = 196$, $Re_{ch} = 1021$, $Re_{ch} = 1895$). The aim of this validation case is to show agreement between pressure and velocity fields with expected results.

The geometry presented by Qu *et al.* [1] is used excluding a plenum at either end of the channel. Assigning a fully developed velocity profile (as described by Qu *et al.* [1]) at the entrance of the channel ensures continuity between the two experiments. The channel dimensions are as follows: $L_{ch} = 120mm$, $H_{ch} = 694\mu m$

and $W_{ch} = 222\mu m$. This geometry is summarized in Table 5.1.

Table 5.1: Channel Dimensions: from the Qu *et al.* [1] geometry

L_{ch}	H_{ch}	W_{ch}
$120mm$	$694\mu m$	$222\mu m$

A non-uniform Cartesian grid was utilized to solve this flow. This grid had uniform grid spacing in the x (flow) direction and non-uniform spacing in the y and z directions with better resolution near the channel walls. The work presented by Qu *et al.* [1] utilized a grid consisting of $160 \times 39 \times 51$ nodes in the x, y and z directions respectively. This work utilized a grid of $300 \times 40 \times 50$ nodes in the x, y and z directions . These grids are comparable because Qu *et al.* [1] used a non-uniform grid in the x direction with better resolution near the inlet and exit, which explains the increased node count in the x direction found in this work. The 600,000 node domain was solved on 10 processors, utilizing parallel processing.

Table 5.1 gives the theoretical and numerical pressure drops through the channel. The application of the velocity profile at the inlet of this work significantly decreases the length of the developing region (the length over which the simulation modifies the velocity profile from the applied profile at the inlet). This truncation of the developing region may explain the difference between the expected and numerical results.

Table 5.2 shows the theoretical and numerical pressure drop through the channel. Good agreement appears between expected and numerical results, showing

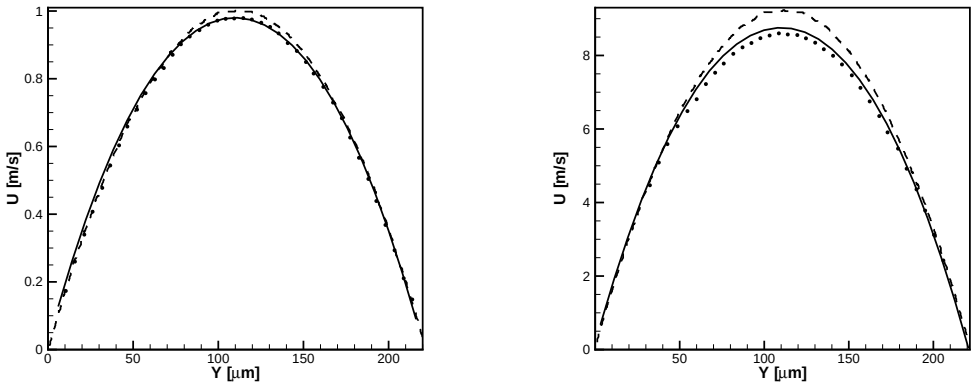

(a) $Re_{ch} = 196, x = 1cm, z = 347\mu m$ (b) $Re_{ch} = 1895, x = 10cm, z = 347\mu m$

Figure 5.1: Velocity profiles at the center plane for different Reynolds numbers and x locations. The solid symbols ($\bullet$) represent experimental data from Qu *et al.* [1], the dashed line ($--$) represents numerical results from Qu *et al.* [1] and the solid line ($-$) represents the work presented. The velocity (U) is given in units of $[m/s]$ and the y location in $[\mu m]$.

Table 5.2: Pressure Drop [bar] through the channel from Qu *et al.* [1]

Re_{ch}	Numerical	Theory
196	0.217	0.200
1021	1.00	1.04
1895	1.91	1.93

small differences for the high Reynolds number cases and a larger error for the low Reynolds number case.

5.2 Flow and Heat Transfer Characteristics of a Heated Pipe

The heat transfer characteristics of the reacting flow is important to resolve the chemical kinetics and species diffusion within the channel. In this work the thermal energy field will be solved and compared to a known solution. The specific heat of the flow is constant. Therefore the thermal energy (enthalpy) field can be directly converted to a temperature field. For the purposes of this validation case a constant specific heat will be assumed and a constant circular pipe cross section will be considered.

To validate the model a circular pipe grid was generated and the governing equations are solved (as seen in Section 3). A uniform flow velocity at the pipe inlet is enforced. The flow allowed to develop and the radial temperature profile was taken in the fully developed region. The criteria to determine the length of the developing region was taken from Incropera *et al.* [36] for laminar flow, as shown in equation 5.1. A no-slip wall boundary condition was enforced at the pipe walls. The pipe exit is set to an outflow condition where the property gradients are zero.

$$x_{fd,t} \approx \frac{Re_D \; Pr \; D}{20} \tag{5.1}$$

Where $x_{fd,t}$ is the developing length for a laminar flow, Re_D is the Reynolds number of the internal flow ($Re_D = UD/\nu$), Pr is the Prandtl number ($Pr = C_p\mu/k$) and D is the pipe diameter.

The grid generated for this validation case is an unstructured quad mesh, generated using a meshing software called Gambit. Figure 3 displays the grid used.

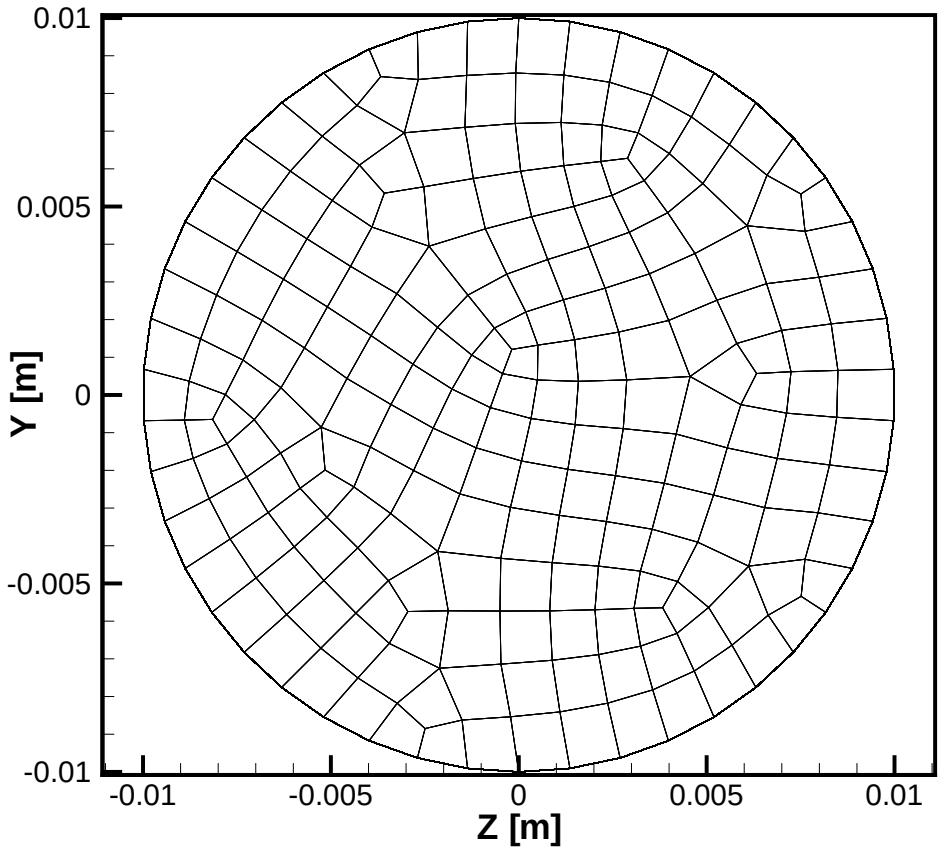

Figure 5.2: Grid used to solve the constant wall temperature pipe flow validation case.

The pipe diameter is 2 cm and the length is 20 cm. The inlet velocity is 0.001 m/s, the acting fluid is water at 20^oC which results in a Reynolds number of 20 and a Prandtl number of 6.62 (properties from [36, 37]). All profile plots are taken from plains extracted from a length greater than 7 diameters from the inlet.

The Hagen-Poiseuille parabolic profile (Figure 5.3) expressing the velocity is given by Kakaç, Shan and Aung [2]. The exact radial velocity profile is given as,

$$u(r) = 2u_m \left(1 - \left(\frac{r}{R}\right)^2\right), \tag{5.2}$$

where $u(r)$ is the local velocity at a given radial distance, r, u_m is the mean velocity, r is the local radial distance, and R is the radius of the pipe. Figure 5.3 gives the velocity profiles from this model and the Hagen-Poiseuille parabolic profile. The profiles are given for laminar flow from a plain within the fully developed region.

Kakaç, Shan and Aung [2] give the radial temperature expression for a fully developed flow in a circular pipe with constant wall temperature. Equation 5.3 gives the expression of the radial temperature for an axial plain,

$$\theta = \frac{T_{wall} - T(r)}{T_{wall} - T_{CL}} = \sum_{n=0}^{\infty} (C_{2n}) \left(\frac{r}{R}\right)^{2n}, \tag{5.3}$$

where,

$$C_0 = 1, \quad C_2 = -\frac{\lambda_0^2}{2^2} = -1.828397, \tag{5.4}$$

$$C_{2n} = -\frac{\lambda_0^2}{n^2} \left(C_{2n-4} - C_{2n-2}\right), \tag{5.5}$$

$$\lambda_0 = 2.7043644199. \tag{5.6}$$

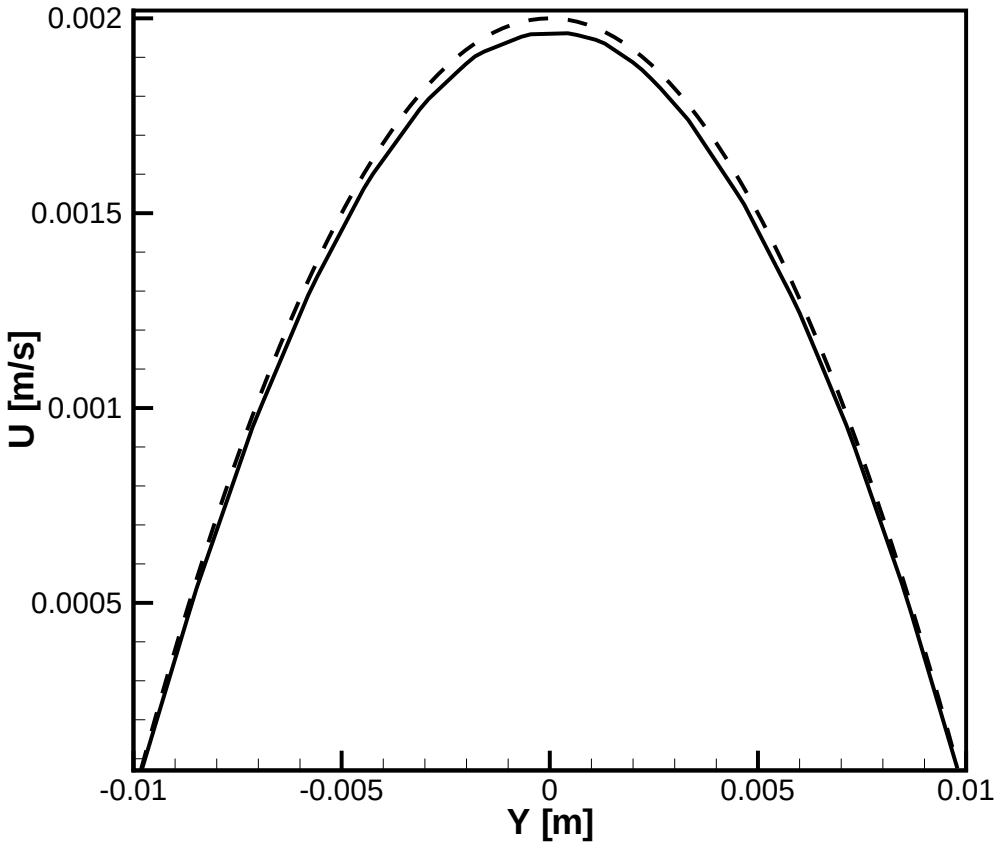

Figure 5.3: Velocity profiles for both the Hagen-Poiseuille parabolic profile [2] and the presented work, for a circular pipe flow. The Hagen-Poiseuille parabolic profile is shown with a dashed line $(--)$ and the profile from this model is shown with a solid line $(-)$.

Here T_{wall} is the constant wall temperature, $T(r)$ is the temperature in the plain investigated at a radial length of r, T_{CL} is the center line temperature. The C values and λ_0 are experimentally-found variables used to calculate the temperature field. Figure 5.4 shows the temperature profile from both this model and Kakaç *et al.* [2].

Good agreement is observed for both the velocity and temperature profiles in the circular pipe between this model and the solutions presented by Kakaç *et al.* [2].

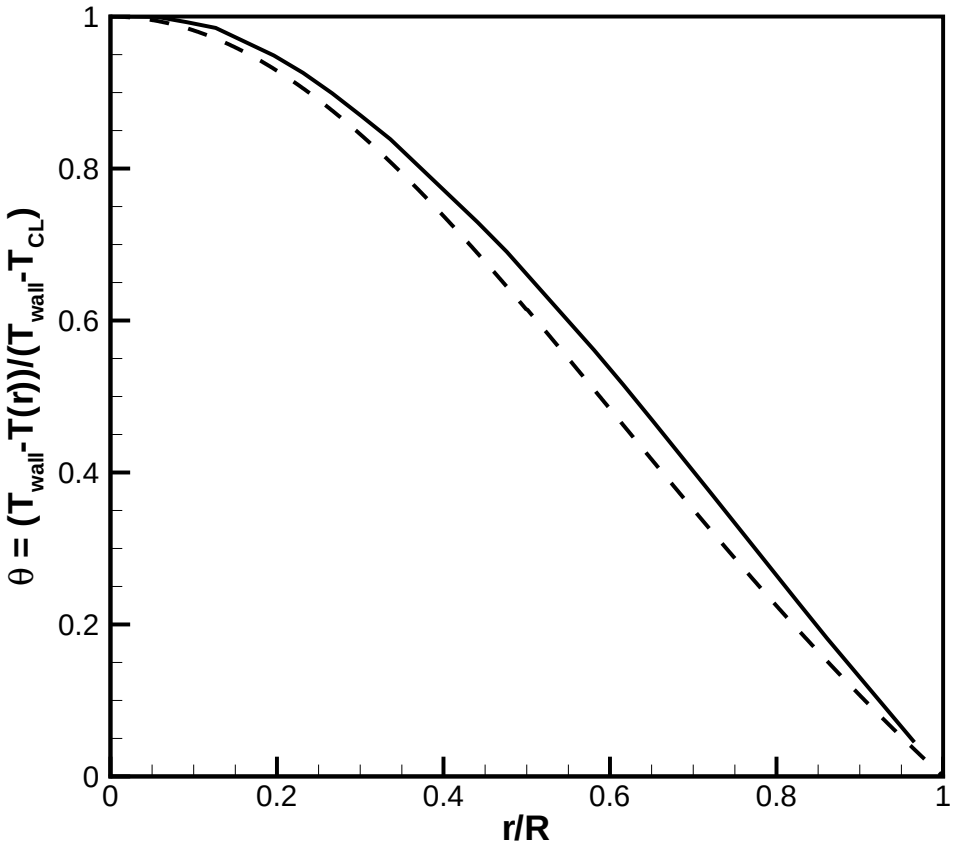

Figure 5.4: Temperature profiles for both Kakaç *et al.* [2] and the presented work are for a circular pipe with constant wall temperature. The Kakaç *et al.* [2] solution is shown with a dashed line $(--)$ and the profile from this model is shown with a solid line $(-)$.

5.3 Reacting Flow

An essential component of solving the mass fraction fields is the correct coupling between the chemical kinetics model and flow solver. Here a heterogenous catalytic reaction is used to validate the coupling of chemical kinetics and flow charactoristics used in this work. This reaction is commonly seen in automobile exhaust gases, when passing over a palladium catalyst. The following results are compared to the exact results presented by Mills [3]. For this case a heterogeneous reaction (which limits the reaction to the catalyst surface) is analyzed, only a one-dimensional model was developed. Here the flow is diffusion driven with a positive concentration gradient, of reactants, from left to right seen in figure 5.5 and the reacting (catalyst) surface is limited to the left wall of the channel. This particular reaction is seen in equation 5.7, where oxygen (O_2) and carbon monoxide (CO) defuse from a rich environment on the right, then react on the catalyst surface producing carbon dioxide (CO_2), which in turn diffuses to the right, see figure 5.5.

The result of this model is the species concentration along the diffusion length (z) of three species considered; carbon dioxide (CO_2), carbon monoxide (CO) and oxygen (O_2). The solving of these concentration gradients are highly dependent on the reaction rate at the catalyst surface, therefore a complete model of the reaction rates must be implemented. Equation 5.8 gives the reaction rate of the catalyst surface as a function of A the pre-exponential constant, E_a the reaction activation energy and T temperature. This form of the reaction rate is known as Arrhenius relation. This model only accounts for a first order reaction but still provides a

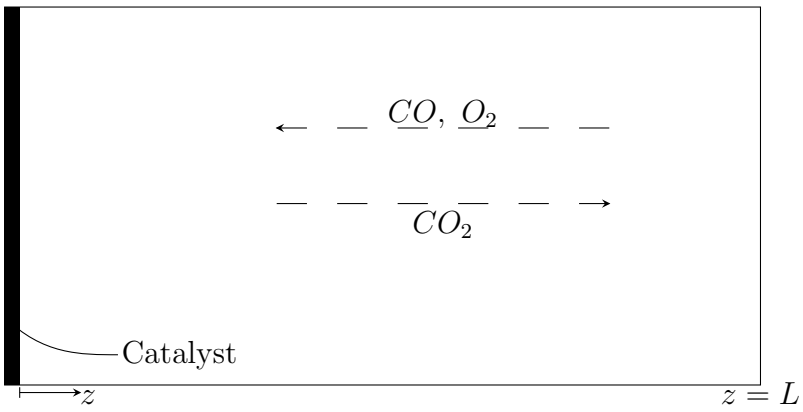

Figure 5.5: Schematic of the flow geometry for the reacting flow validation case. Where the reactants diffuse from right to left, react on the catalyst wall and the products diffuse from left to right. Carbon dioxide (CO_2) has a rich concentration at the catalyst (left) wall and oxegen (O_2) and carbon monoxide (CO) are in rich concnetration at the inlet (right boundary).

valuable validation study.

$$2CO + O_2 \rightarrow 2CO_2 \tag{5.7}$$

$$k = Aexp\left(\frac{-E_a}{RT}\right), \tag{5.8}$$

where; k is the reaction coefficient which has units of $[m/s]$; A is the pre-exponential constant which is typically found experimentally, and is forced to take the same units as k $[m/s]$; E_a is the activation energy for this reaction with units of $[kJ/kmol]$; R is the universal gas constant with units of $[kJ - K/kmol]$ and T is the temperature in $[K]$.

This model only considers catalytic reactions, therefore the gas phase chemical kinetics are assumed negligible (no homogeneous reactions). This allows the chem-

ical kinetics to be collapsed into a boundary condition. Performing a mass balance at the catalyst surface gives the boundary condition found in equation 5.9. The cross flow boundary conditions are periodic, given the one-dimensional nature of this model.

$$\rho D_i \frac{dm_i}{dz}\bigg|_{catalyst} = k\rho m_i\bigg|_{catalyst}, \tag{5.9}$$

where; ρ is the mixture density taking units of $[kg/m^3]$, D_i is the mass diffusion coefficient of the i^{th} species with units of $[m^2/s]$, m_i is the mass concentration of the i^{th} species which is treated as dimensionless, but takes units of $[kg_i/kg_{mix}]$, z is the length in the diffusion direction, in units of $[m]$ and k is discuses above.

Governing Equation:

$$\rho\frac{\partial m_i}{\partial t} + \rho\frac{\partial}{\partial z}(um_i) = \rho\frac{\partial}{\partial z}\left(D_i\frac{\partial m_i}{\partial z}\right) + \dot{s}_{si} \tag{5.10}$$

Gas Phase:

$$\rho D_i \frac{dm_i}{dz} = 0 \tag{5.11}$$

Catalyst Surface:

$$\rho D_i \frac{dm_i}{dz} = -\dot{s}_{si} \tag{5.12}$$

Where, the bold text represents a vector such that, $\mathbf{u}$ is the velocity vector; t is time in $[sec]$ and s_{si} is a mass source term which describes the mass of species i production or consumption as a function of the reaction rate.

The governing equation for this reaction is conservation of chemical species,

written in full form in equation 5.10. After assuming a steady state solution (no time dependence), diffusion driven (no velocity term), applying to one dimension and rearranging the governing equation and applying to the gas phase (no reaction) gives equation 5.11; and when applied to the catalyst surface the equation becomes 5.12. The final expression of the governing equation is in agreement with the catalyst boundary condition equation 5.9 and the mass balance preformed at the catalyst wall. Given these boundary conditions and governing equation 5.11 can be integrated twice with respect to z, to provide the concentration gradients in the diffusion (z) direction, which is expressed in linear form, in equation 5.13. After applying the boundary conditions to equation 5.13 and normalizing the mass concentration of the i^{th} component with the i^{th} component mass concentration at the inlet (for O_2 and CO), one recovers a mass concentration equation as a function of z. Reaction characteristics and geometry are summarized in table 5.3. The exact concentration gradient is given in equation 5.14. The results of both the exact solution and numerical simulation are shown in figure 5.6. Here one can see good agreement between the expected results and numerical results.

$$m_i = C_{1_i} z + C_{2_i} \tag{5.13}$$

$$\frac{m_i}{m_{i,e}} = \frac{1 + \frac{kz}{D_i}}{1 + \frac{kL}{D_i}} \tag{5.14}$$

The grid used to solve is uniform Cartesian in the cross diffusion direction and non-uniform Cartesian in the z direction with fine resolution near the catalyst wall.

Table 5.3: Reaction characteristics from Mills [3]

k	1.179×10^{-3}	m/s
ρ	0.442	kg/m^3
D_{CO}	97.8×10^{-6}	m^2/s
L	0.1	m

The chemical kinetics and flow charactoristics are summarized in table 5.3. The activation energy (E_a) and pre-exponential constant (A) are not given because the catalyst wall is assumed isothermal and a constant reaction coefficient (k) is given. This model was solved on a three-dimensional grid, because this model is only one-dimensional the x and y boundary conditions are periodic. The solution was found to be grid independent.

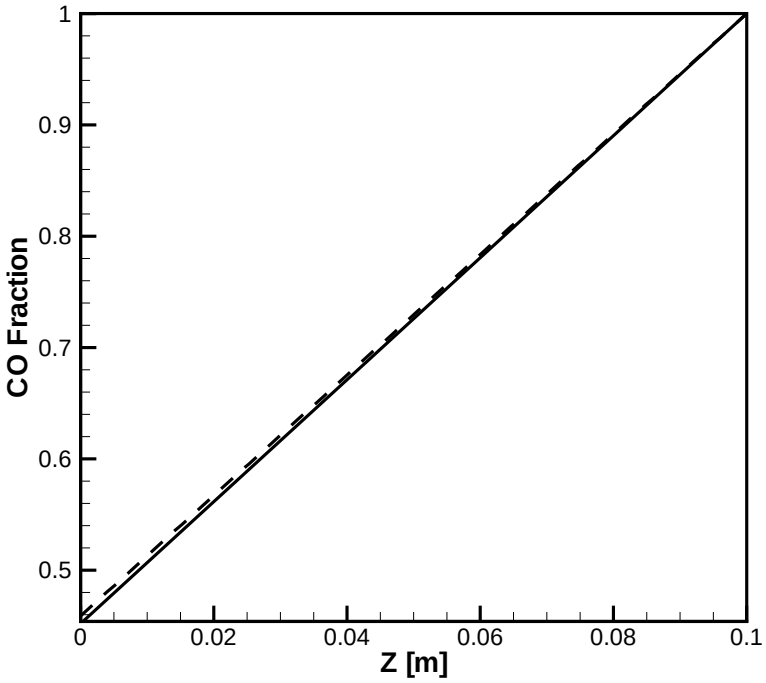

Figure 5.6: Mass fraction of carbon monoxide (CO) normalized with the CO mass fraction at the inlet, in the z (diffusion) direction expressed in units of $[m]$. The exact solution given by Mills [3] is shown by a dashed line ($--$) and the work presented here is show with a solid line ($-$).

5.4 Chemical Kinetics Model

Reaction rates verification was completed to validate this chosen chemical kinetics model. The species mass fraction fields are solved by imposing a species mass fraction boundary condition, which is directly related to the chemical reaction rates. Here the predicted reaction rates are compared to those found by Kuznetsov & Kozlov [4].

Kuznetsov *et al.* [4] investigated two heat flux profiles, five heat flux magnitudes and two channel geometries. All reaction rate profiles were given for both heat flux profiles, one heat flux magnitude ($\overline{q} = 2\ kW/m^2$), and one geometry (height of $0.5\ mm$ and length of $0.1125\ m$). Accordingly, the validation here will investigate those two reactor heat flux profiles (uniform and ramp). The channel has an entry length, without catalyst, of 30 height lengths. The heat flux is applied only to the catalyst section (leaving the entry length unheated).

The two heat flux profiles considered are uniform and nonuniform (ramp). The uniform heat flux forces a constant heat flux of $\overline{q} = 2\ kW/m^2$, along the catalyst length. The nonuniform (ramp) heat flux varies the heat flux linearly along the catalyst length. The heat flux profile of the nonuniform case starts at $0\ kW/m^2$ at the start of the catalyst section, and grows linearly to twice the mean heat flux, $4\ kW/m^2$ (for the $\overline{q} = 2\ kW/m^2$ case). All other reactor parameters (total heat input, reactor geometry, steam-methane ratio and flow rate) were kept constant for these validation trials .

Figure 5.7 gives the reaction rates of all three reactions considered along the

reactor length with a uniform heat flux profile. All three reaction rate profiles agree well with Kuznetsov *et al.* [4]. The chemical kinetics models used by Kuznetsov [4] and in the presented work are vastly different (see Section 2). Acknowledging the variations between the reaction rates are explained. The reaction rates for both the Kuznetsov [4] model and the presented model are given in Figure 5.7. The species molar fraction for both models are given in Figure 5.8. This figure shows excellent agreement between the Kuznetsov model and the model presented in this work. The exit concentrations of all species are directly related to the area under the reaction rate curves. The closer agreement of the mole fractions profile than the reaction rate profiles, indicates the reaction rate areas of the two models are approximately equivalent. The reaction rate profiles support this inference .

The same study was performed for the nonuniform (ramp) heat flux profile. Similar plots are generated and are seen in Figures 5.9 and 5.10. The reaction rates for both models are seen in Figure 5.9, where the second and third reaction rates profiles compare well to those predicted by the Kusnetsov model [4]. While the local reaction rate of the first reaction varies between these two models, the mole fraction profiles compare very well. Figure 5.10 gives the species concentrations (on a molar basis) for both models. Both models compare well.

The experimental data for variations of mole fraction along the channel length are not available. Therefore, evaluating the physical accuracy of either model is difficult. While the exit mole fractions are available which provide no assistance in choosing between models because the exit mole fraction of those models .

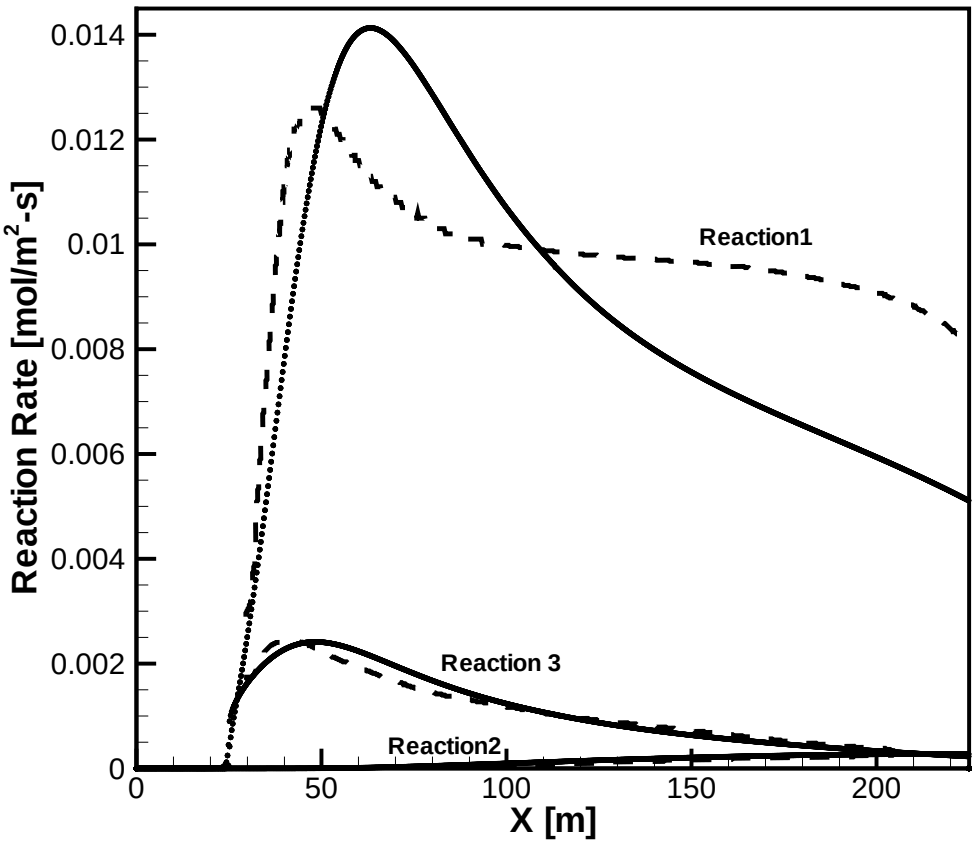

Figure 5.7: Reaction rates profiles for all three reactions considered here. For a uniform heat flux of 2 kW/m^2. The Kuznetsov model [4] predictions are shown with dashed lines $(--)$ and the predictions of this model are shown with solid lines $(-)$. The three reactions are denoted.

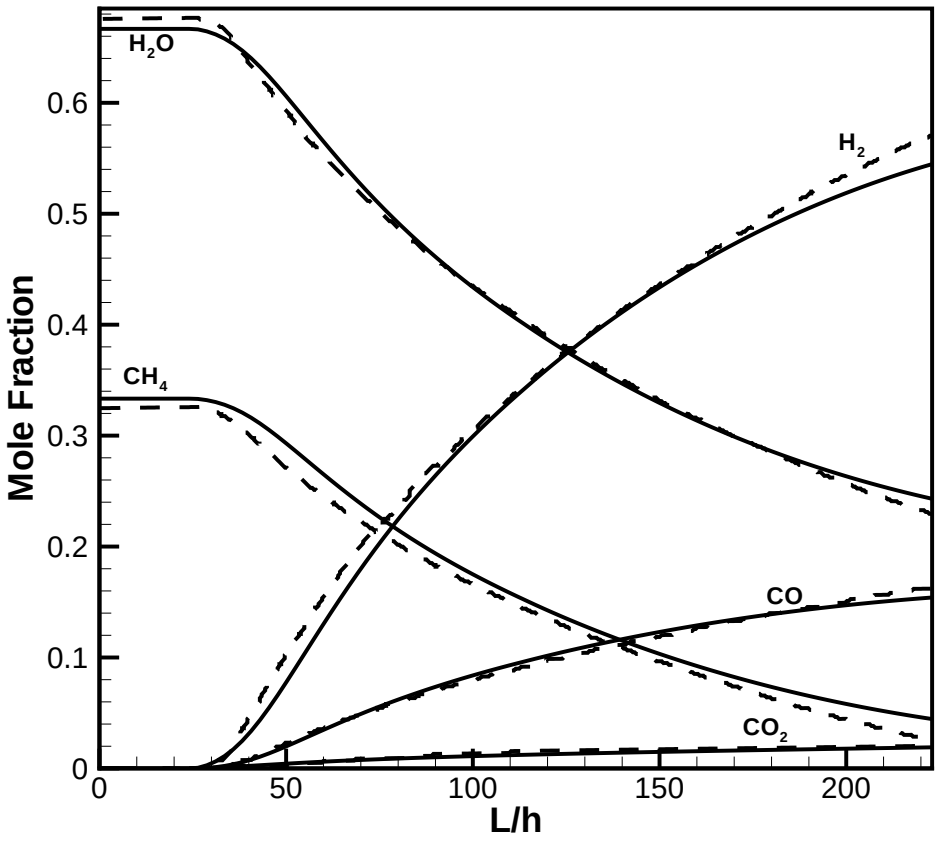

Figure 5.8: Species mole fraction profiles along the channel length for a uniform heat flux of 2 kW/m^2. Here the Kuznetsov model [4] predictions are shown with dashed lines $(--)$ and the predictions of this model are shown with solid lines $(-)$. The different chemical species are denoted.

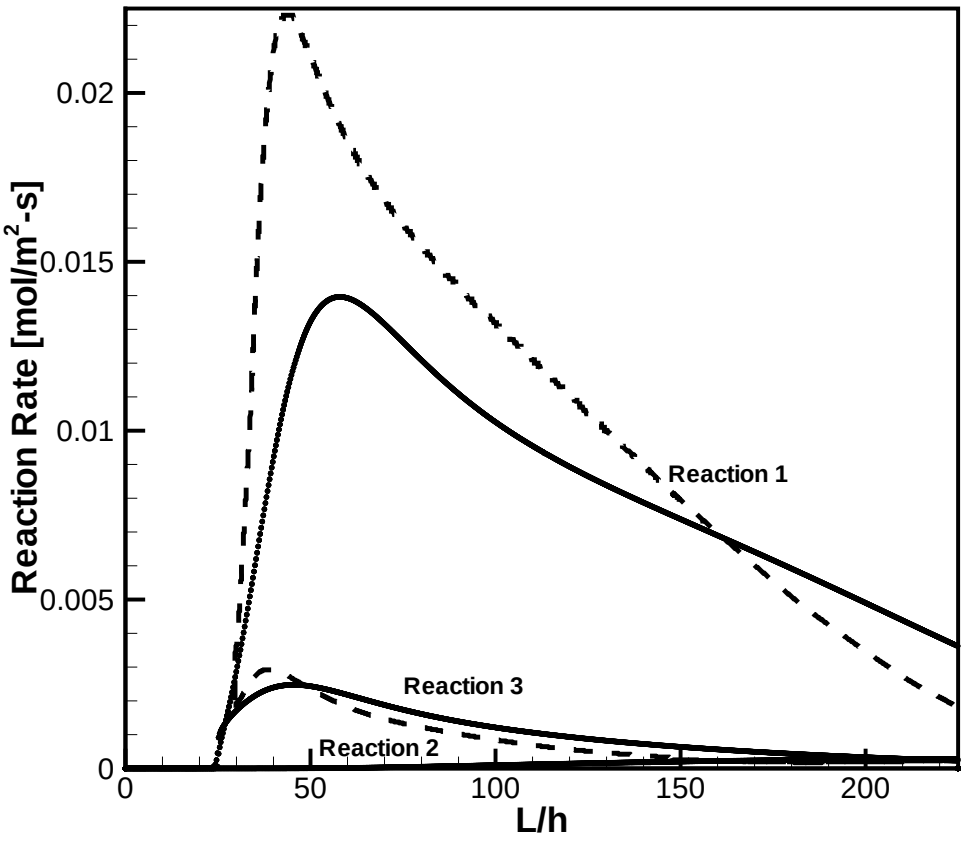

Figure 5.9: Reaction rates profiles for all three reactions considered here for a ramped heat flux with average magnitude of 2 kW/m^2. The Kuznetsov model [4] predictions are shown with dashed lines $(--)$ and the predictions of this model are shown with solid lines $(-)$. The three reactions are denoted.

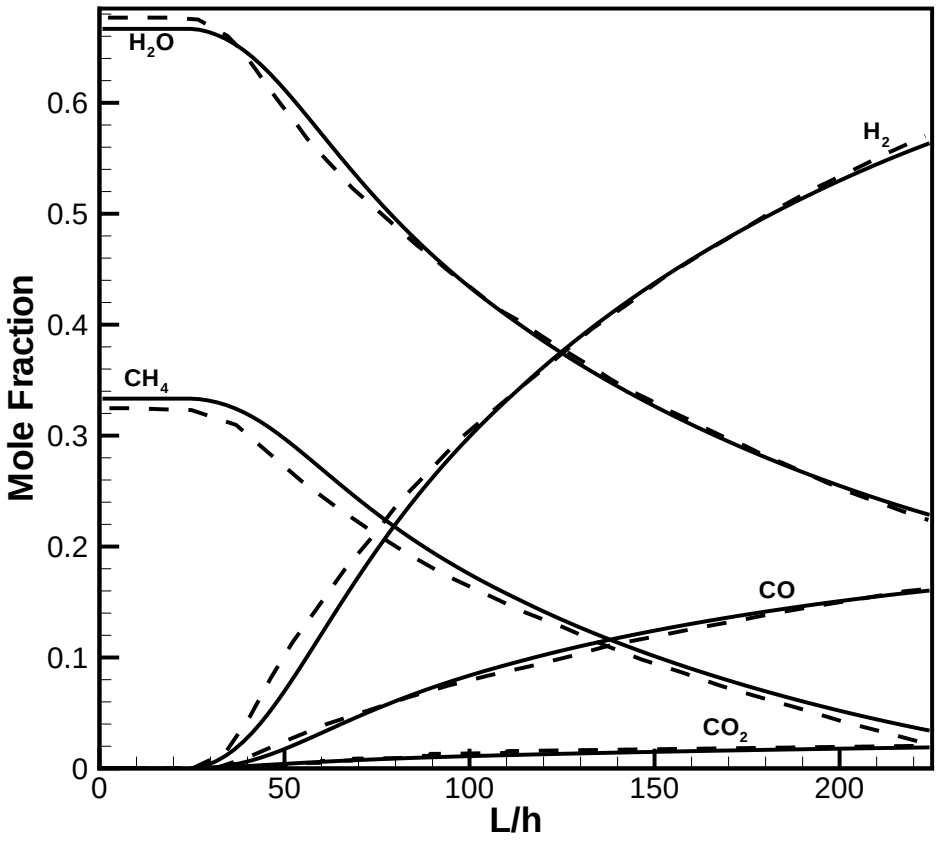

Figure 5.10: Species mole fraction profiles along the channel length, for a ramped heat flux with average magnitude of 2 kW/m^2. Here the Kuznetsov model [4] predictions are shown with dashed lines $(--)$ and the predictions of this model are shown with solid lines $(-)$. The different chemical species are denoted.

Chapter 6 – Results

The boundary conditions detailed in previous sections are collected in Table 6.1. These boundary conditions are used for all simulations. A uniform inlet velocity field (based on the flow-rate and inlet area) together with Dirichlet conditions for the species mass fractions (based on the steam-methane ratio) are specified. A convective boundary condition is imposed at the outlet section. No-slip conditions are assumed on the walls. For regions with no catalyst, a zero-flux Neumann condition is employed for the species mass-fractions and temperature fields. For the catalyst region, the species mass-fractions and temperature conditions are based on the catalytic reactions (equation 4.17). The Z edges are handled as periodic, which truncates the wall effects.

Table 6.1: Boundary conditions used in simulations

Boundary	Velocity	Species	Temperature
Inlet	$\mathbf{U} = (U_{inlet}, 0, 0)$	$Y_i = Y_{i,inlet}$	$T = T_{inlet}$
Exit	$\frac{\partial \mathbf{U}}{\partial n} = 0$	$\frac{\partial Y_i}{\partial n} = 0$	$\frac{\partial T}{\partial n} = 0$
Catalyst	$\mathbf{U} = 0$	$\frac{\partial Y_i}{\partial n} = \frac{-\dot{s}_i \mathcal{M}_i}{\rho \mathcal{D}_i}$	$\frac{\partial T}{\partial n} = \frac{-q_{wall} - \sum_k r_k \Delta H_{R,k}}{k}$
Walls	$\mathbf{U} = 0$	$\frac{\partial Y_i}{\partial n} = 0$	$\frac{\partial T}{\partial n} = 0$
Z Edges	$\Phi(x, y, -\delta) = \Phi(x, y, \delta)$		
where $\Phi = \mathbf{U},\ Y_i$ *and* T			

There are three geometries considered here, those found in the works by Eilers [38], Wang *et al.* [5] and Kuznetsov *et al.* [4]. All of these geometries are described my Figure 6 and Table 6.2.

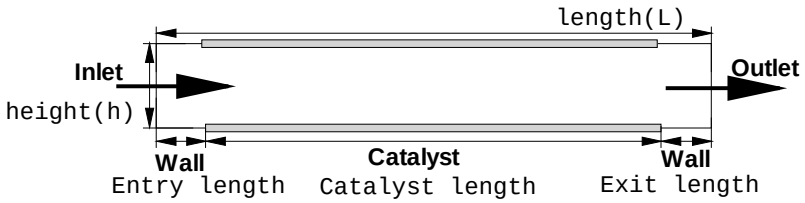

Figure 6.1: Schematic of the microchannel reactor.

Table 6.2: Geometry Dimensions of the three channel studied

	Height	Length	Entry Length	Catalyst Length
	mm	mm	mm	mm
Eilers* [38]	0.86	133.35	0	133.35
Wang *et al.* [5]	4.5	130	15	100
Kuznetsov *et al.* [4]	0.5	112.5	30	82.5

* The Eilers geometry [38] has catalyst only on the bottom wall.

6.1 Methane-Steam Reformations

A full model of the methane steam reformation was validated with the work by Wang *et al.* [5]. Wang investigated the effects of steam methane inlet ratio flow rates on hydrogen production, operating pressure, and wall temperature. The channel considered has dimensions of 4.5 mm in height and 0.13 m in total length with a catalyst section of 0.1 m centered in the middle of the channel length. This geometry is captured in Figure 6.2.

To validate the numerical methods used in this work the results simulated by Wang *et al.*[5] were replicated. A simple uniform Cartesian mesh is used to capture the flow geometry as specified above. Here a two-dimensional solution was generated with 25 control volumes (CVs) along the height (flow normal direction) and 800 CVs in the flow direction.

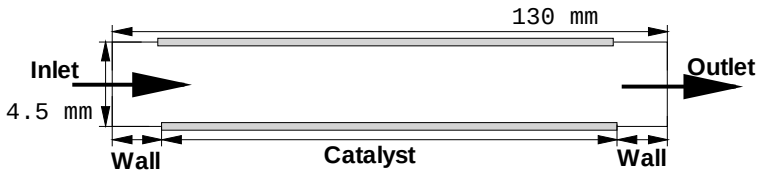

Figure 6.2: Schematic of the microchannel reactor with catalyst on the top and bottom surfaces.

After the mesh was generated, the porous activation factor was found. Accurate characterization of the reaction on the catalyst surface is critical to correctly predict the chemical conversion in the microchannel reactor. Given the complexity of the surface reaction mechanisms in the presence of a porous catalyst, it is difficult to

completely model the diffusion and chemical reactions through the porous surface. The reaction rates predicted by the equations 1.1, 1.2 and 1.3 for a non-porous catalyst are calibrated against the experimental data from Wang *et al.* [5]. These reaction rates are then used to predict the hydrogen production for different cases studied by Wang *et al.* [5] good agreement with the experimental data is shown. This model requires a scaling term (catalyst activation factor) to be introduced to scale the reaction rates. The scaling term characterizes the effects of the porous catalyst as shown in the following equation:

$$r_1 = C_a k_1 \left(\frac{\rho}{\mathcal{M}_{CH_4}}\right)\left(\frac{\rho}{\mathcal{M}_{H_2O}}\right) Y_{CH_4} Y_{H_2O}, \tag{6.1}$$

$$\mathrm{r_2 = C_a k_2 \left(\frac{\rho}{\mathcal{M}_{CO}}\right)\left(\frac{\rho}{\mathcal{M}_{H_2O}}\right) Y_{CO} Y_{H_2O}}, \tag{6.2}$$

$$\mathrm{r_3 = C_a k_3 \left(\frac{\rho}{\mathcal{M}_{CH_4}}\right)\left(\frac{\rho}{\mathcal{M}_{H_2O}}\right)^2 Y_{CH_4} Y_{H_2O}^2}. \tag{6.3}$$

The porous activation factor is iteratively found. The simulation was run completely with the porous activation factor set to a value of one. Then, the bulk mean hydrogen molar concentration is found by using the following equation:

$$Y_{bulk,H_2} = \frac{1}{A_c \overline{u}} \int_A u Y_{H_2} dA. \tag{6.4}$$

This bulk mean concentration was then corrected to give a molar concentration of dry exit gases. The dry concentration was found so that it could be compared to experimental results (which require the analyzed gases to be free of water).

The simulated hydrogen concentration is compared to the experimentally found hydrogen concentration. The ratio of these two results (experimental concentration and numerical concentration) is then used to correct the activation factor. This method assumes in each iteration a linear relationship between the catalyst activation factor and the exit hydrogen concentration. While this relationship is highly nonlinear, the iterative nature of this method converges on an appropriate activation factor.

The results were all validated using varying total inlet flow rates of $\dot{Q} = 100,\ 200,\ 300,\ 400,\ 800\ ml/min$. All other operating conditions are held at the following constants: steam-methane ratio of 2.5, wall temperature of 973 K, and operating pressure of 110 kPa. The results were examined by using two methods. First the lengthwise concentrations (molar fraction) of the hydrogen and methane were compared. Figure 6.3 gives the local molar fraction of hydrogen for three of the five flow rates for both the work presented by Wang [5] and this study. In both cases the concentrations are taken along the channel length near the catalyst wall. The sharp decline of molar fraction after the catalyst section is explained by a rapid diffusion of hydrogen with the bulk flow. While the exact trend differs between the two studies, Figure 6.3 shows the total hydrogen molar fraction compares well.

Figure 6.4 gives the local molar fraction of methane for three flow rates for both the work presented by Wang *et al.* [5] and this study. Figure 6.4 also shows the concentrations taken along the channel length near the catalyst wall. The sharp increase of methane molar fraction after the catalyst section is also explained by

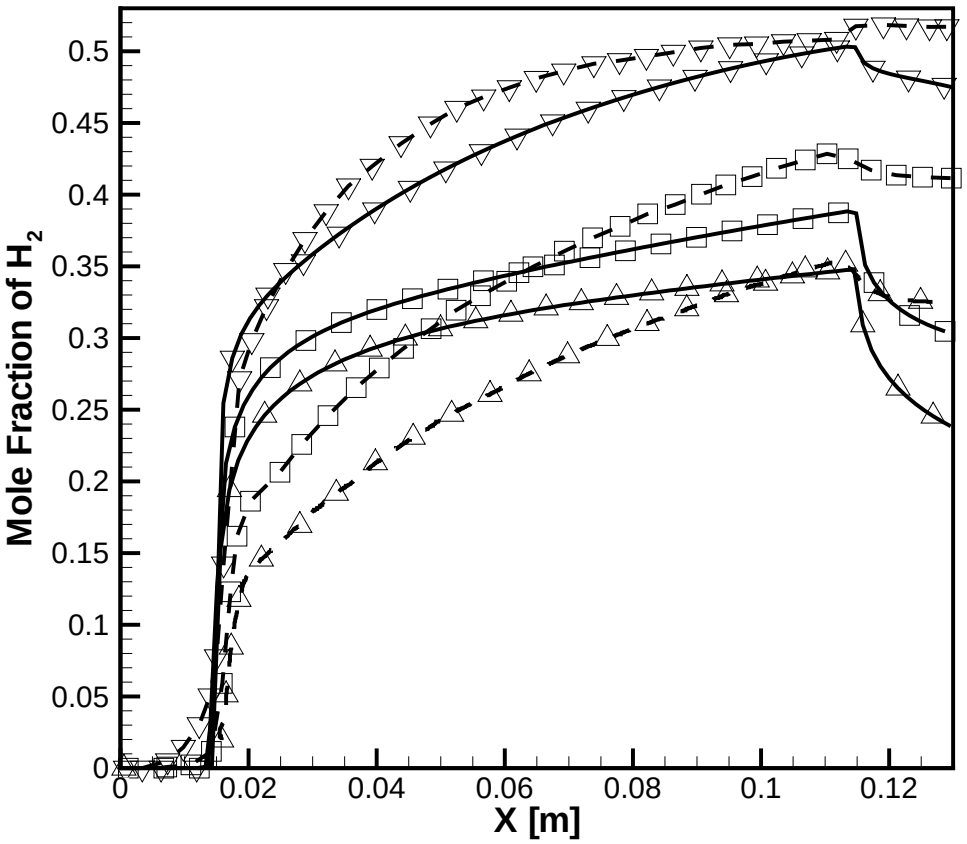

Figure 6.3: Production of hydrogen as a molar fraction along the channel length. Here the solid lines $(-)$ represent the presented work and the dashed lines $(--)$ represent the Wang *et al.* [5] predictions for three flow rates: 100 ml/min shown with downward triangles, 300 ml/min with squares and 800 ml/min with upward triangles.

a rapid diffusion, where methane diffuses to the catalyst surface from the bulk.

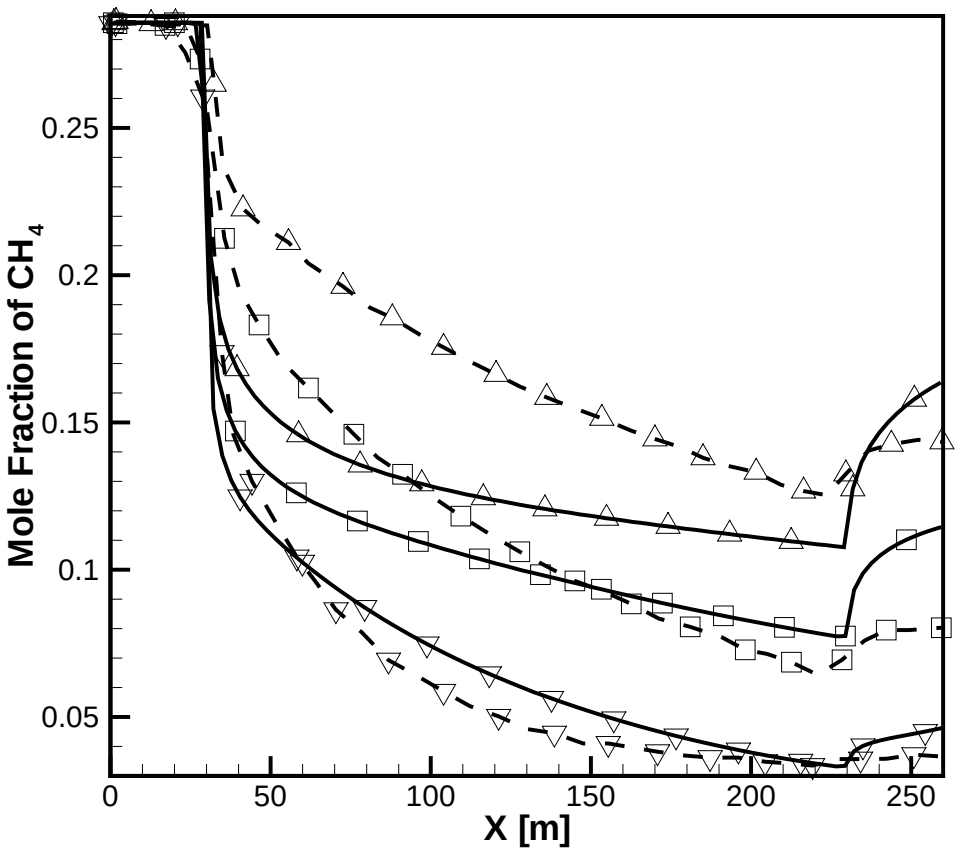

Figure 6.4: Depletion of methane as a molar fraction along the channel length. Here the solid lines ($-$) represent the presented work and the dashed lines ($--$) represent the Wang *et al.* [5] predictions for three flow rates: 100 ml/min shown with downward triangles, 300 ml/min with squares and 800 ml/min with upward triangles.

Good agreement is seen between the results calculated by this kinetics model and that used in [5, 4]. Table 6.3, shows the concentration (molar fraction) of

hydrogen at the end of the catalyst section (near the catalyst section in the y direction). The percent difference for all five flow rates is less than 10%. The hydrogen concentration is taken at the end of the catalyst section and not the end of the channel, to minimize errors introduced by different diffusion effects. Taking the concentration near the catalyst section at the end of the catalyst measures the kinetics rather than the diffusion model.

Table 6.3: Hydrogen Production Compared to Wang *et al.* [5] Results

Flow Rate ml/min	Wang H_2 Production Molar Fraction	Peterson H_2 Production Molar Fraction	Percent Difference %
100	0.515	0.503	2.36
200	0.486	0.444	9.05
300	0.451	0.412	9.04
400	0.423	0.400	5.59
800	0.343	0.348	1.45

Table 6.4, gives the consumption of methane for both studies. Again, the percent difference is given between the results found by Wang *et al.* [5] and those found here. Four of the flow rates agree within 5% and the other is within 12%. Here the near catalyst conversion of methane is considered. This gives a measure of how complete the reaction is at the end of the catalyst section. While the methane conversion is a good measure of the reaction completion, it may not offer a good measure of overall optimization of parameters. The desired result is a high volume flow rate of hydrogen, which is the product of the bulk mean hydrogen concentration and the flow rate.

Table 6.4: Methane consumption Compared to Wang *et al.* [5] Results

Flow Rate	Wang CH_4 Percent Consumption	Peterson CH_4 Percent Consumption	Percent Difference
ml/min	%	%	%
100	87.5	89.0	0.559
200	81.5	78.0	4.21
300	75.2	73.3	2.50
400	67.5	69.9	3.57
800	53.5	59.7	11.1

The computational domain with the height and spanwise length of 4.5 mm and axial flow length of 0.13 m. A porous Nickel catalyst section, on the top and bottom walls, starts at flow length of 0.015 m and continues up to 0.115 m. This catalyst configuration allows the flow to develop before the reaction zone. The Reynolds number varies between simulations but is always in the laminar flow regime. A Cartesian grid was used in this simulation with 25×800 control volumes in the vertical and axial directions, respectively. For the present study, variations in spanwise directions are assumed negligible and a two-dimensional configuration is also assumed.

In this zero-Mach number variable density reacting flow model, the reactor pressure is assumed constant at 100 kPa. The inlet temperature is set to 973 K for all cases. The total heat flux ($|\dot{q}''|$), the heat flux profile ($\dot{q}'' = f(x)$), the inlet steam-methane ratio (S:M), and the inlet flow rate ($\dot{Q}$) are varied and their effects on hydrogen production are investigated.

The effect of the parameters studied here are compared in three ways: (1) hydrogen mole fraction at the end of the reactor length, (2) methane conversion at the end of the catalyst and (3) chemical species concentrations' development along the reactor length. The hydrogen mole fraction is considered as the primary measure to evaluate the effect of parameter studies. The conversion of methane is considered to give a measure of the completeness of combustion. The development of the chemical species along the reactor length is considered to compare the behavior within the reactors.

6.2 Heat Flux Magnitude

Heat flux magnitude and hydrogen production are directly correlated. The reaction rates are highly dependent on temperature. Accordingly, increased heat flux improves performance. The effects of heat flux magnitude is seen in Figure 6.5 where the mole fraction of hydrogen is seen along the reactor length. This section applies the variation in heat flux magnitude to the ramp up case, where the heat flux grows linearly from zero at the start of the catalyst to twice the average heat flux at the end of the catalyst.

The methane conversion is considered in Figure 6.6. The conversion percent increases with increased heat flux. The increase in methane conversion percent correlates to more complete combustion.

Figure 6.7 shows the concentration of all species studied along the reactor length. The heat flux condition plotted is that of the best performing, $q'' = 3\ kW/m^2$.

6.3 Flow Rate

Figure 6.8 shows the dominant reaction rate for different flow rates. For lower flow rates, and thus with increased convective residence time, the reactions near completion and the majority of the methane is consumed to produce hydrogen as expected.

As discussed previously, the reaction rates are highly dependent on the local temperature. Here, we investigate the effect of external heat flux on hydrogen

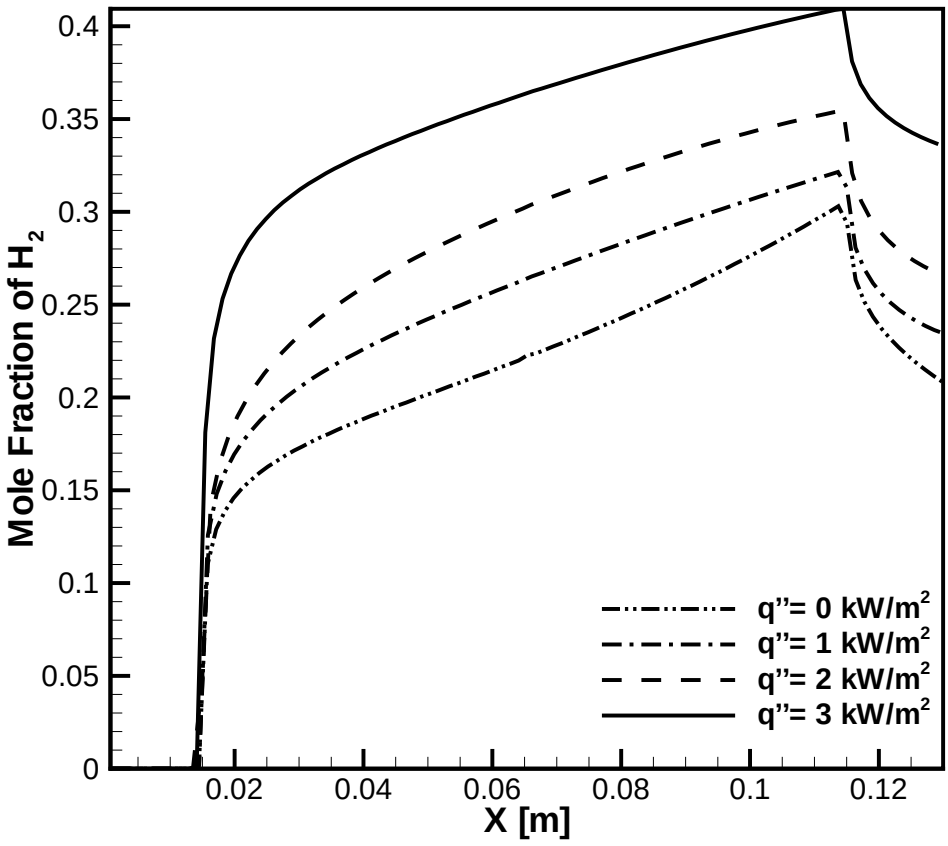

Figure 6.5: Variation of H_2 concentration along the microchannel reactor for different wall heat flux magnitudes. The flow rate is 400 ml/min; the steam-methane ratio is 2.5; and the constant wall temperature is 973 K

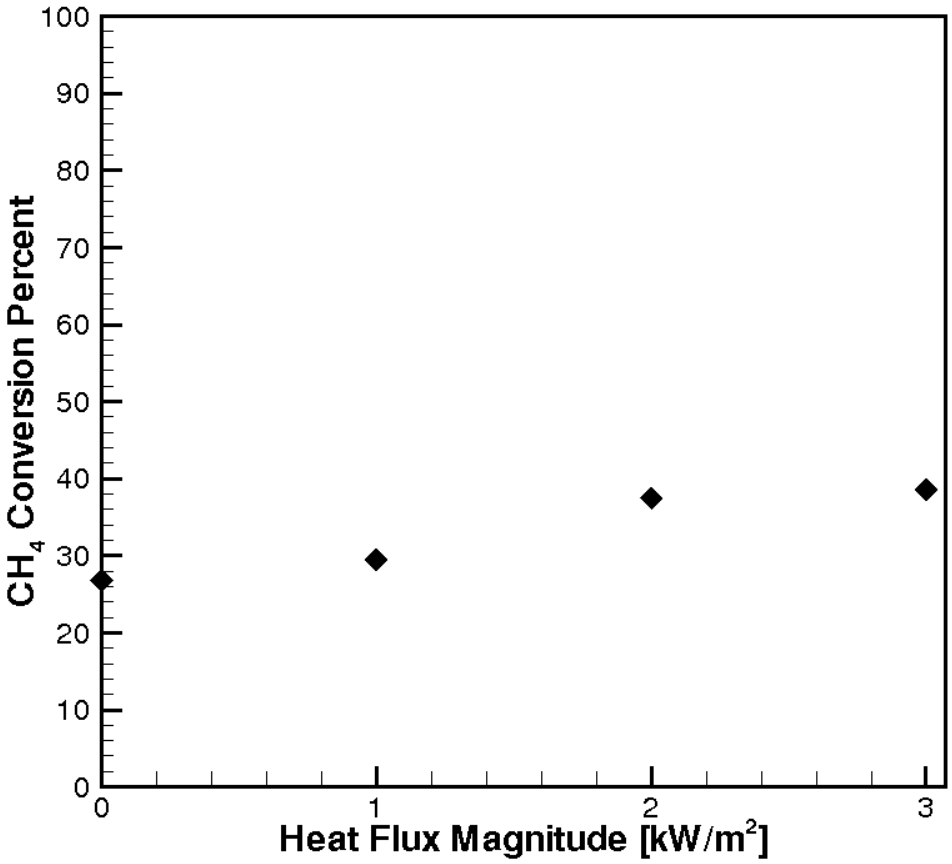

Figure 6.6: Methane conversion along the microchannel reactor for different wall heat flux magnitudes. The flow rate is 400 ml/min; the steam-methane ratio is 2.5; and the constant wall temperature is 973 K

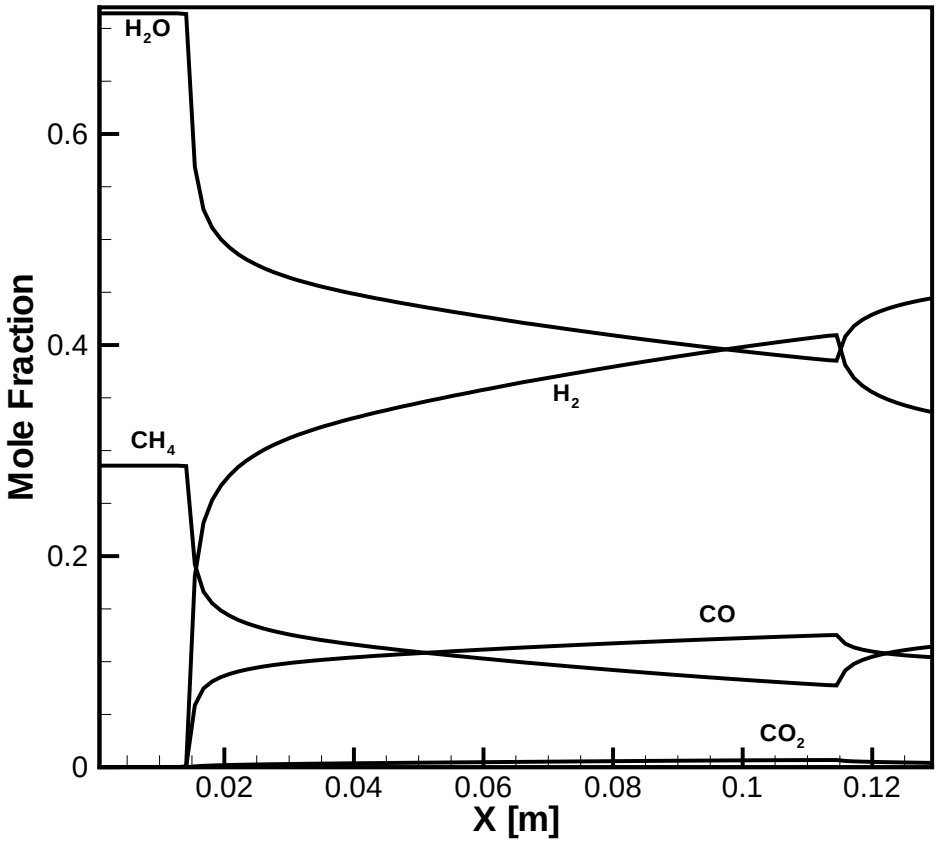

Figure 6.7: Chemical species mole fraction along the microchannel reactor for a wall heat flux magnitudes of $q'' = 3\ kW/m^2$. The flow rate is 400 ml/min; the steam-methane ratio is 2.5; and the constant wall temperature is 973 K

.

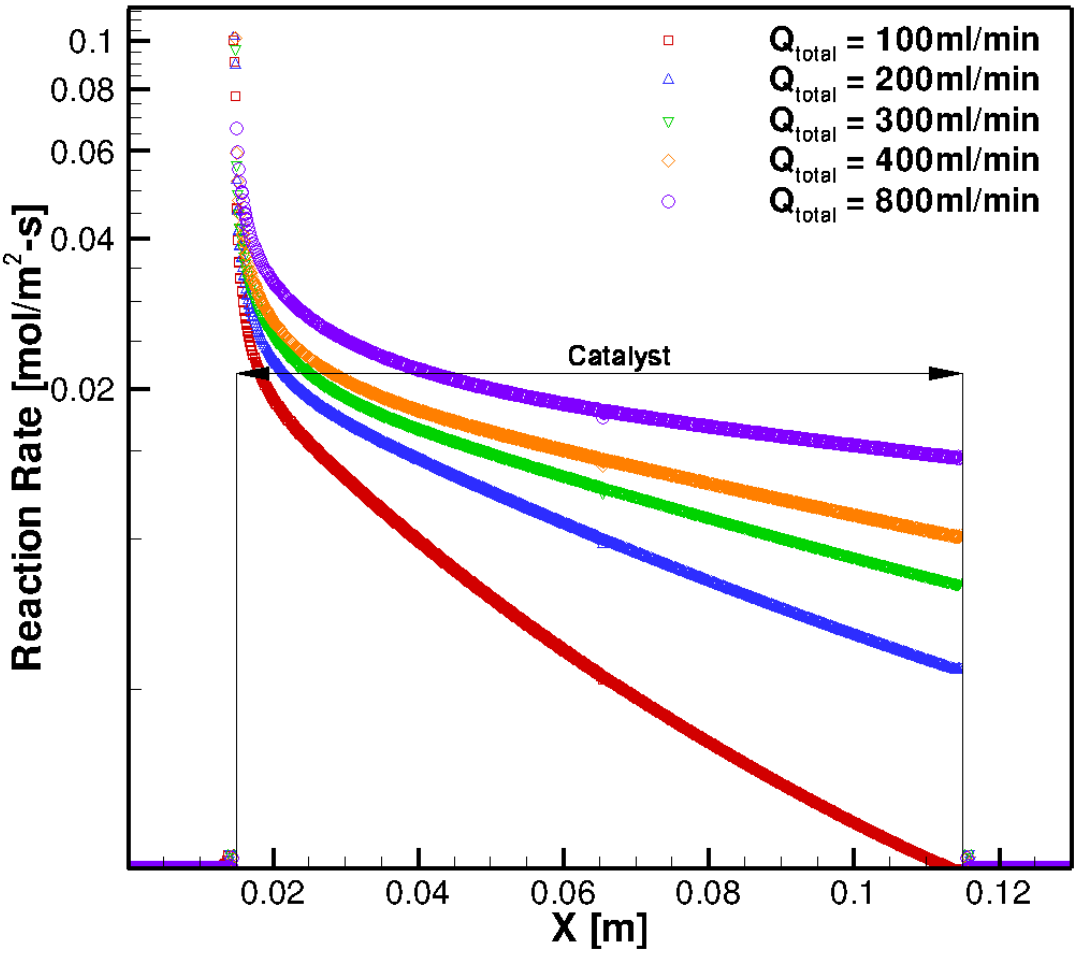

Figure 6.8: Variation of surface reaction rates for different flow rates and a steam-methane ratio of 2.5 with constant wall temperature of 973 K.

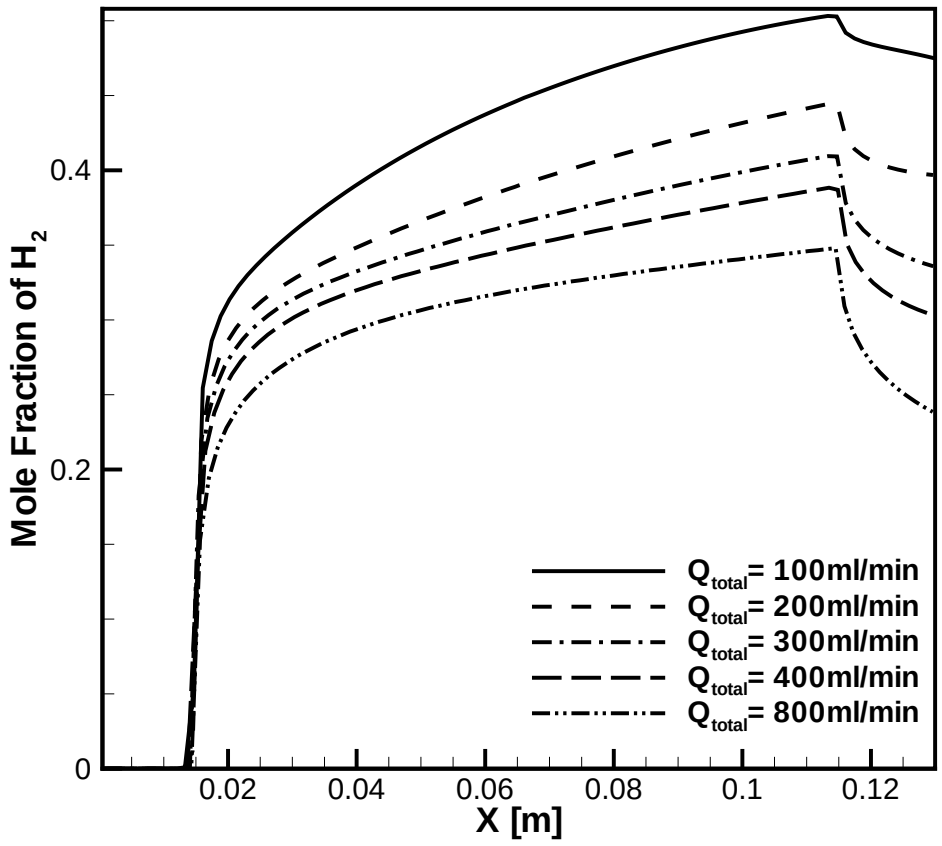

Figure 6.9: Variation of H_2 concentration along the microchannel reactor for different flow rates. The steam-methane ratio is 2.5; the heat flux profile is ramp up; and the constant wall temperature is 973 K

production. Four heat flux magnitudes were enforced at mean values of 0, 1, 2 and 3 kW/m^2. The heat flux is also linearly increasing along the channel wall. The steam-methane ratio is set to 2.5 and the flow rate for these cases is maintained at $400ml/min$. It is found that increasing heat flux results in increased hydrogen production and reaction rates. Increasing the value of heat flux increases the temperature along the wall, leading to enhanced hydrogen production. The reaction rates plot indicates a peak in their values at the beginning of the catalyst surface. The premixed methane-steam mixture diffuses to the catalyst surface and reacts to produce hydrogen. Production of hydrogen is an endothermic reaction, and this causes the temperature at the wall to initially decrease. Reactions continue to occur along the channel wall, however their rate is decreased. The amount of methane and steam diffusing to the channel wall are also affected with production of hydrogen in the upstream section. Since the inlet temperature of the premixed mixture is relatively high, reactions are initiated even for the case of no heat flux. However, the amount of hydrogen produced is considerably lower compared to high heat flux cases (see Figure 6.5). The variation of hydrogen molar fraction shows a decrease after the catalyst section. This decrease is mainly because of diffusion of hydrogen produced at the wall to the centerline of the channel. Regardless, the bulk hydrogen molar fraction remains the same after the catalyst section.

The methane conversion is given in Figure 6.11, which shows that the conversion percent increases with decreasing flow rate. The increase in methane conversion percent correlates with longer resident times which allow for more complete combustion. Figure 6.10 shows the concentration of all species studied along the

reactor length. The flow rate condition plotted is that of the best performing flow rate, $Q_{total} = \ 100\ ml/min$.

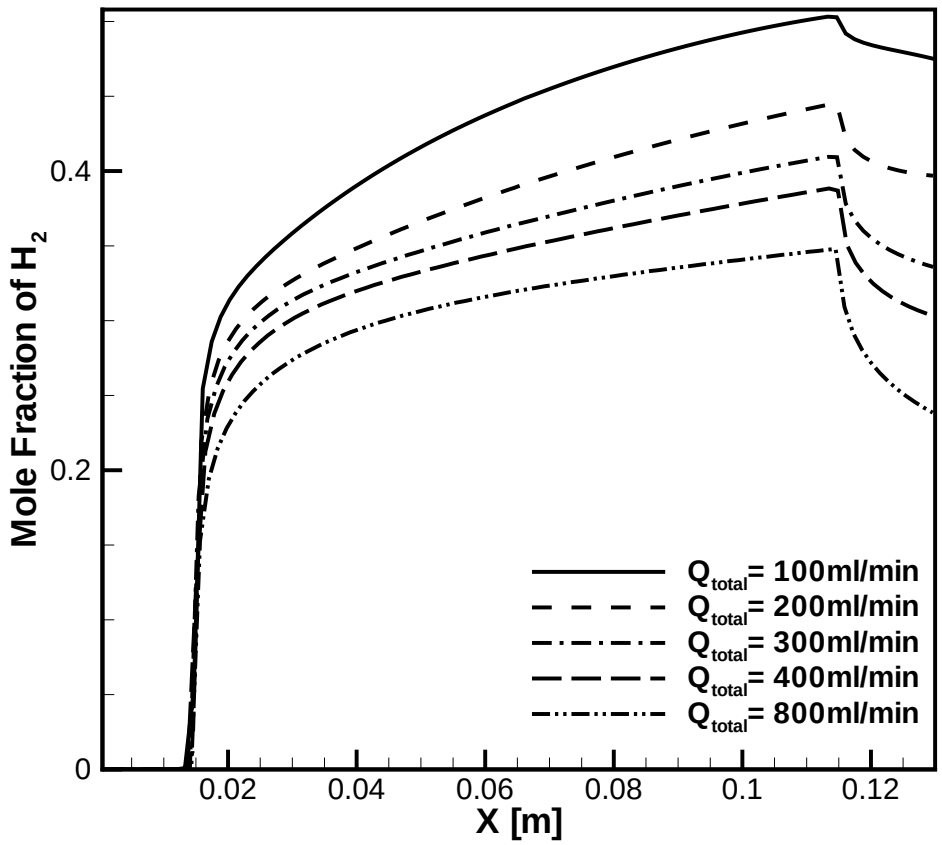

Figure 6.10: Chemical species mole fraction along the microchannel reactor for a total flow rate of $Q_{total} = 100\ lm/min$.

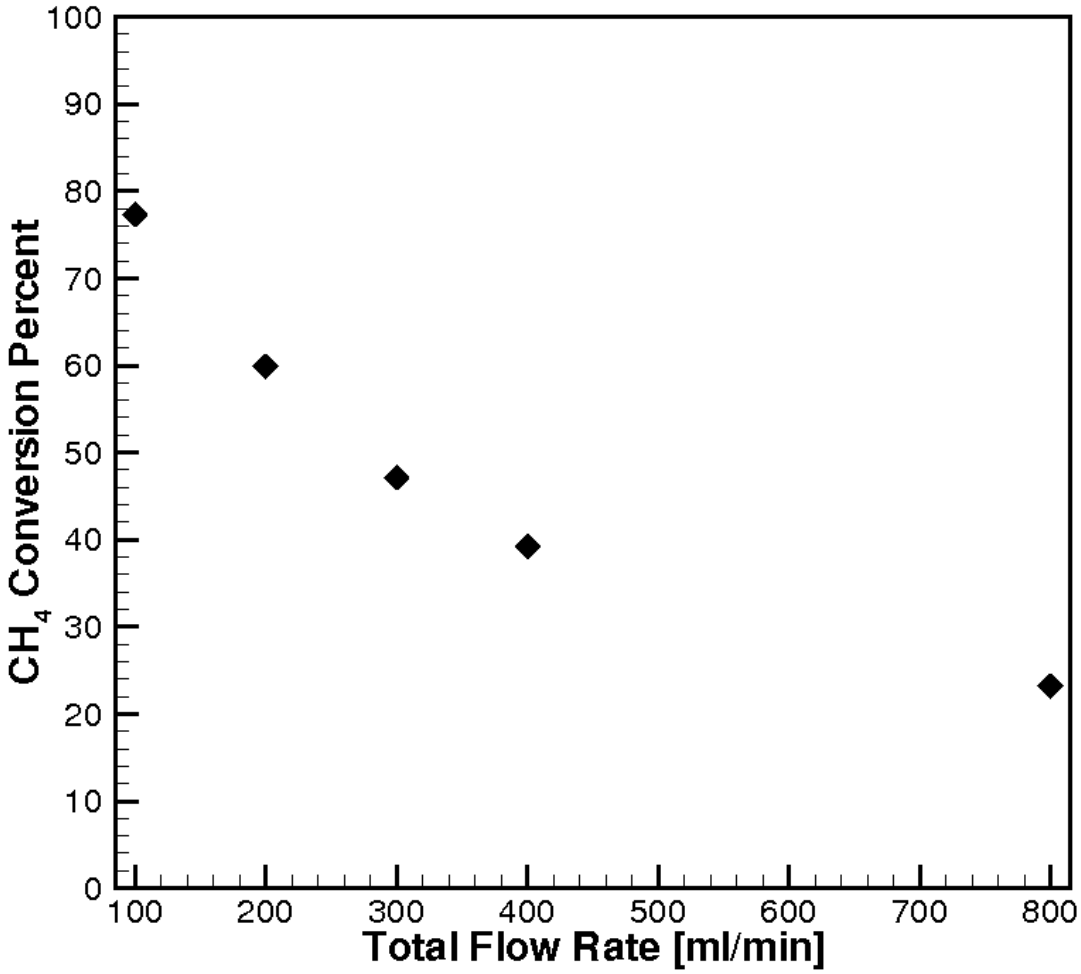

Figure 6.11: Methane conversion along the microchannel reactor for different flow rates.

6.4 Heat Flux Profile

Since methane-steam reforming is an endothermic reaction, the temperature values near the catalyst drops in the absence of heat addition. In order to explore the effect of heat-flux profile on the non-linear nature of the reaction rates and hydrogen production, this study considers three different heat flux profiles: uniform distribution, ramp up, and ramp down wherein the heat flux varies linearly along the channel walls. For all cases, the average heat flux over the reactor length is kept fixed at 2 kW/m^2 and the steam-methane ratio is set to 2.5 at a flow rate of $400ml/min$.

Figures 6.12 and 6.13 show the variation of hydrogen molar concentrations along the channel together with wall temperature for the three different heat flux profiles. It is observed that, for all heat flux profiles, the temperature drops in the upstream section of the channel where the reaction rates are large. The ramp down heating, however, does not raise the temperature of the wall sufficiently to produce higher hydrogen concentrations. Small increases in temperature occur mainly because the endothermic reaction rates are smaller and also there is heat addition. The ramp-up distribution seems to give increased production of hydrogen. It should be noted that in the present microchannel, the conversion of methane is not complete for the flow rate of 400 ml/min. This indicates that a longer microchannel is needed for complete conversion.

The methane conversion is shown in Figure 6.15. The conversion percent is highest for the ramp up profile, less for the uniform profile and least for the ramp

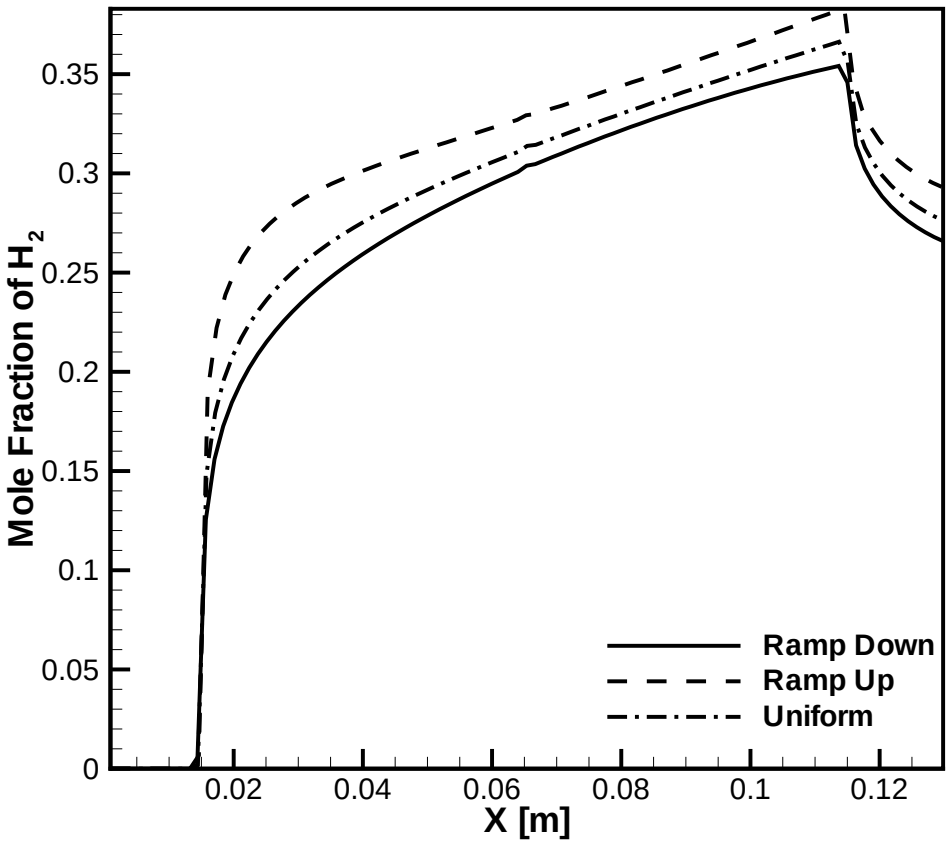

Figure 6.12: Variation of H_2 molar concentration along the channel wall for different heat flux profiles. The average heat flux is kept constant at 2 kW/m^2; the flow rate is 400 ml/min; and the steam-methane ratio is 2.5.

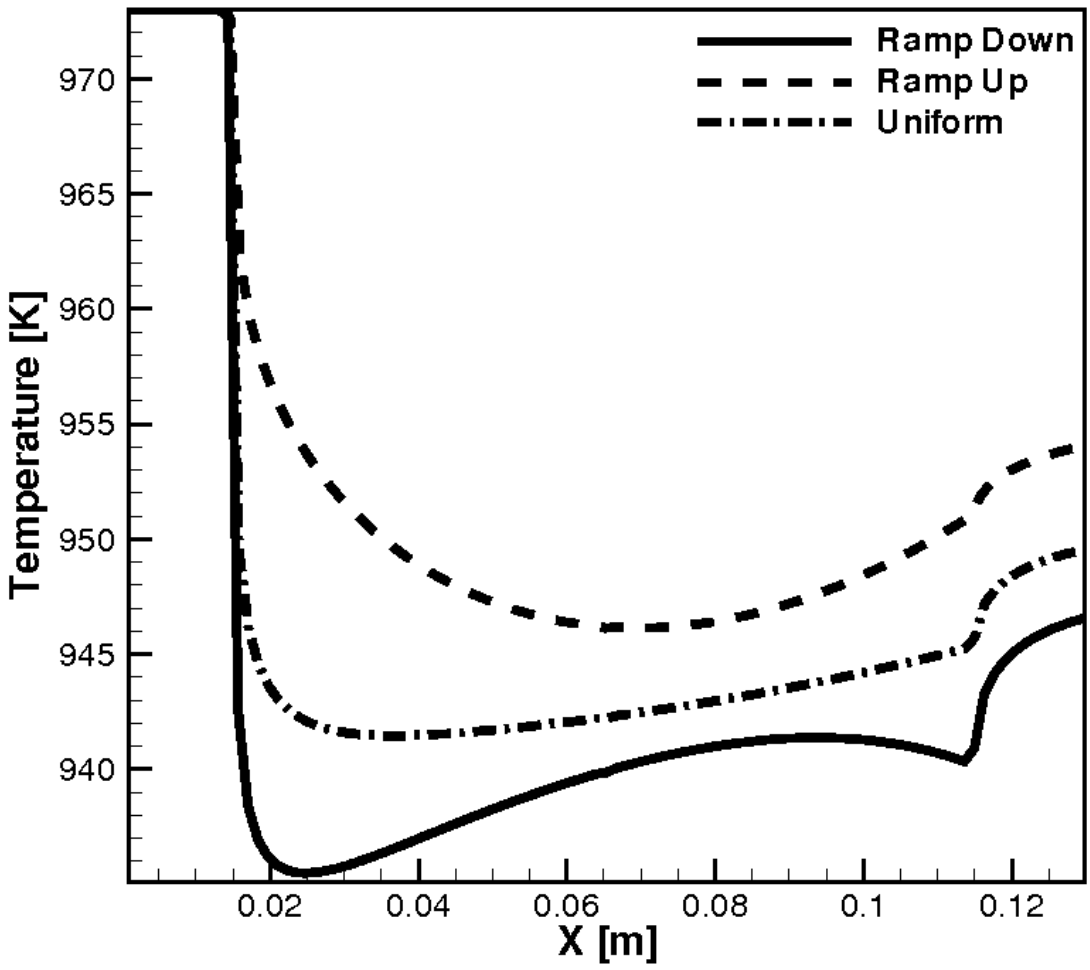

Figure 6.13: Variation of H_2 of wall temperature along the channel wall for different heat flux profiles. The average heat flux is kept constant at 2 kW/m^2; the flow rate is 400 ml/min; and the steam-methane ratio is 2.5.

down profile. The increase in methane conversion percent correlates with increased average reaction rates. The reaction rates are driven by the high reactant concentrations near the start of the catalyst. In addition, the high temperature drives the reaction rates near the end of the catalyst. Inputting the bulk of the energy where the reactant concentrations are low allows for better conversion at a given average heat flux. Figure 6.14 shows the concentration of all species studied along the reactor length. The heat flux profile condition plotted is that of the best performing heat flux profile, ramp up profile.

6.5 Steam Methane Ratio

The inlet steam-methane ratio for a flow rate of 400 ml/min and average heat flux of 2 kW/m^2. The heat flux profile is linear ramp up along the channel wall. The reaction rates are non-linear functions of the reactant concentrations. It was found that a steam-methane ratio of approximately 3.0 (on molar basis) provides the maximum hydrogen production as shown in Figure 6.16.

The methane conversion is given in Figure 6.17 which shows the conversion percent is nonlinear related to the steam-methane ratio. The complex and highly nonlinear relationship between the system performance and steam-methane ratio is investigated for a number of ratios. For ratios above 4 and below 1 the methane conversion percent decreased and will not be detailed here. Figure 6.18 shows the concentration of all species studied along the reactor length. The steam-methane ratio condition plotted is that of the best performing ratio, $S : M = 3$.

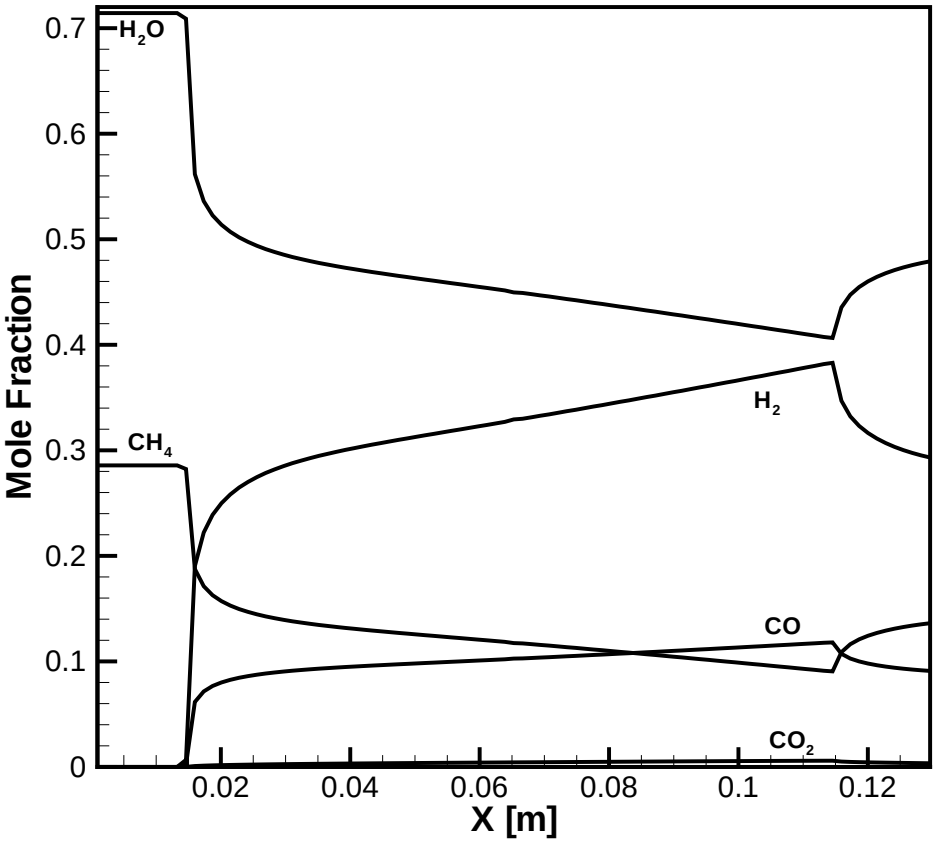

Figure 6.14: Chemical species mole fraction along the microchannel reactor for a heat flux profile of ramp up and average magnitude of $q'' = 2\ kW/m^2$.

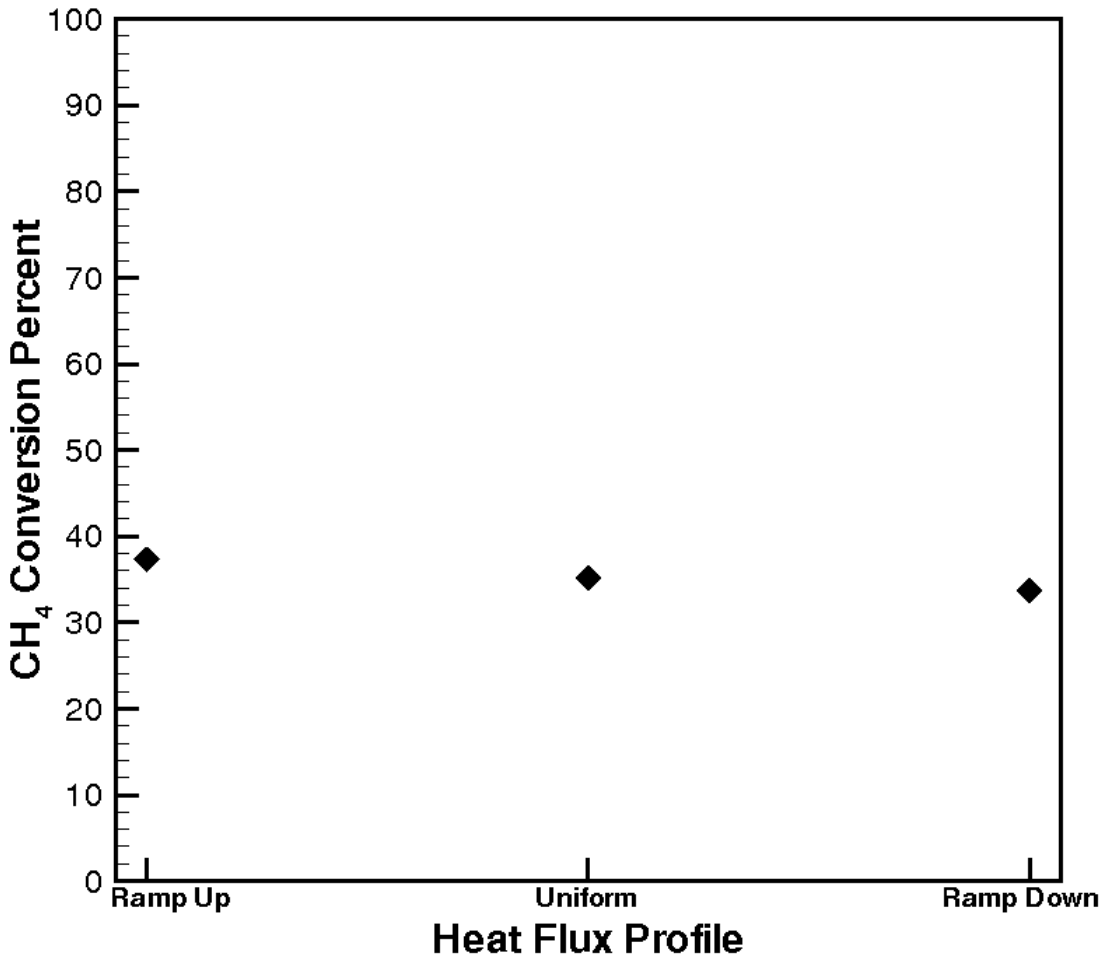

Figure 6.15: Methane conversion along the microchannel reactor for different heat flux profiles.

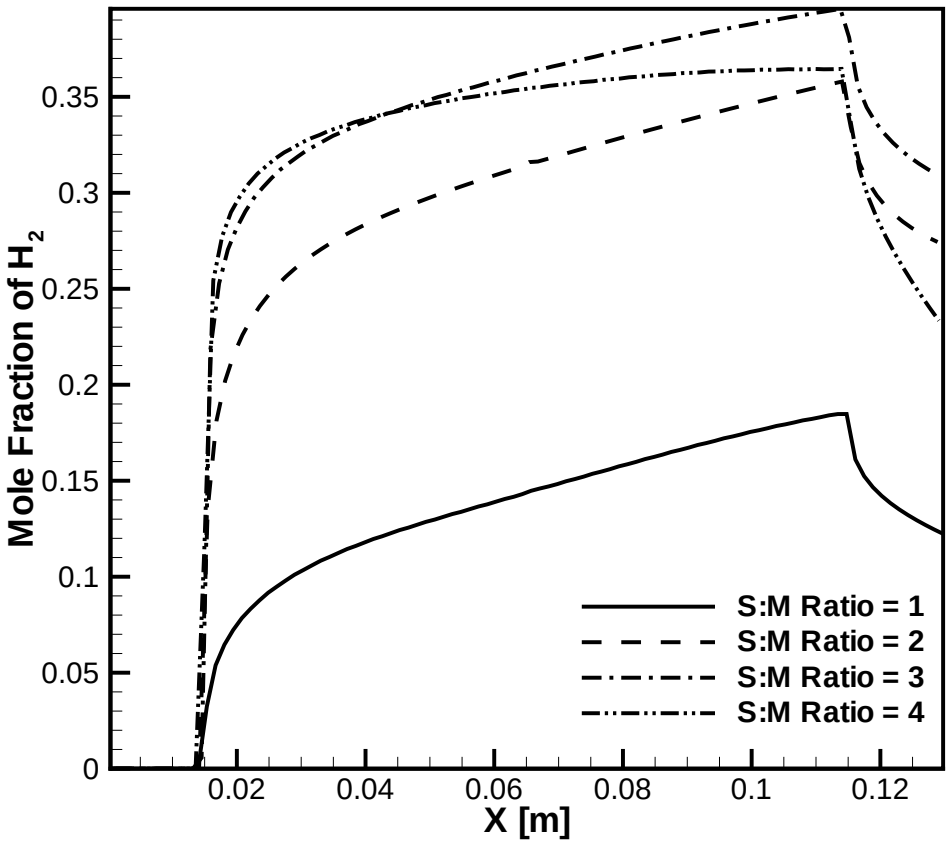

Figure 6.16: Variation of H_2 molar concentration along the channel wall for different steam-methane ratios. The wall temperature is kept constant at 973 K and the flow rate is 400 ml/min.

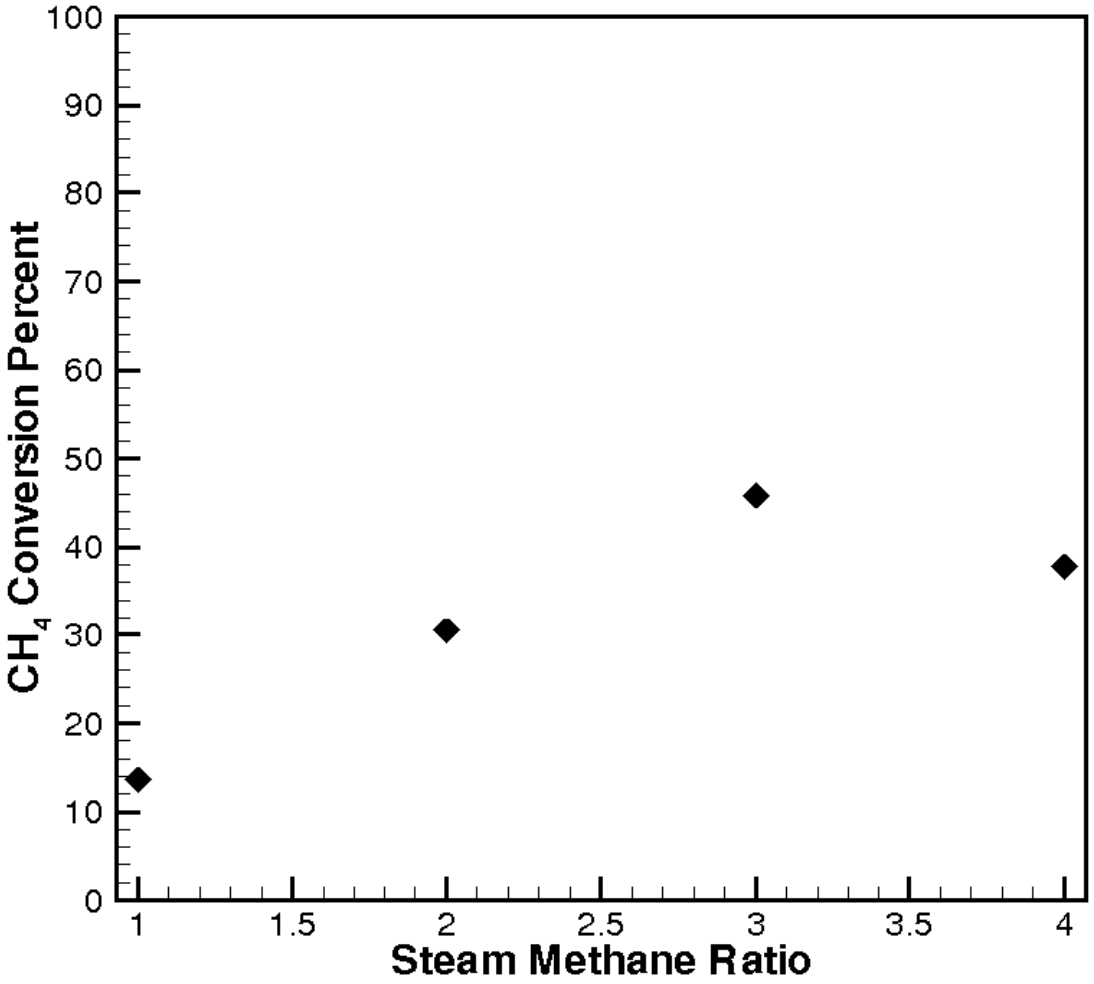

Figure 6.17: Methane conversion along the microchannel reactor for different inlet steam-methane ratio.

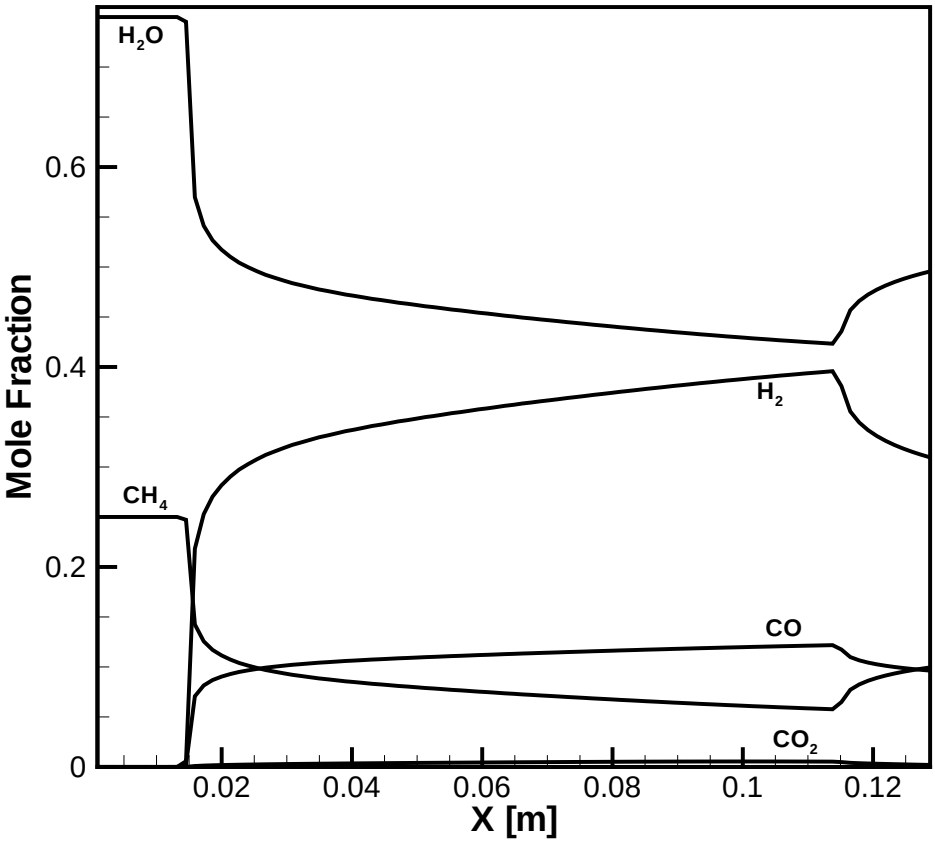

Figure 6.18: Chemical species mole fraction along the microchannel reactor for a steam-methane ratio of 3.

6.6 Experimental Facility

The numerical model used in this work was developed in parallel with an experimental facility. The results from the experiments are used to validate and refine the numerical model. Three operating parameters are considered to validate the model: pressure drop through the device (validates the meshing of the geometry), velocity profile (allows for the simplification of the modeled geometry and flow solver), and exit species concentrations (validates the chemical kinetics model).

The simulation geometry is seen is Figure 6.19. A downward velocity at the inlet of the left pipe is enforced and an outflow condition on the end of the right pipe is also enforced. The top section of the left pipe is 0.073 m long with a diameter of 0.0046 m. The bottom section is 0.013 m long with a diameter of 0.0032 m. The top section of the the right pipe is 0.061 m long with a diameter of 0.0046 m. The bottom section is 0.013 m long with a diameter of 0.0032 m. The height of the channel is 0.86 mm with a total length of 0.1735 m and a catalyst length of 0.13335 m. The width of the channel is 19 mm in the catalyst section. All walls were given a no-slip condition.

The mesh generated at the bottom of the channel was extruded in the z direction to produce the three dimensional mesh used to solve the flow fields as shown in Figure 6.20.

The pressure drop through the device was measured experimentally and modeled numerically. The geometry is given in Figure 6.19. The pressure drop is measured between ends of the two circular pipes shown. Nitrogen gas was used as

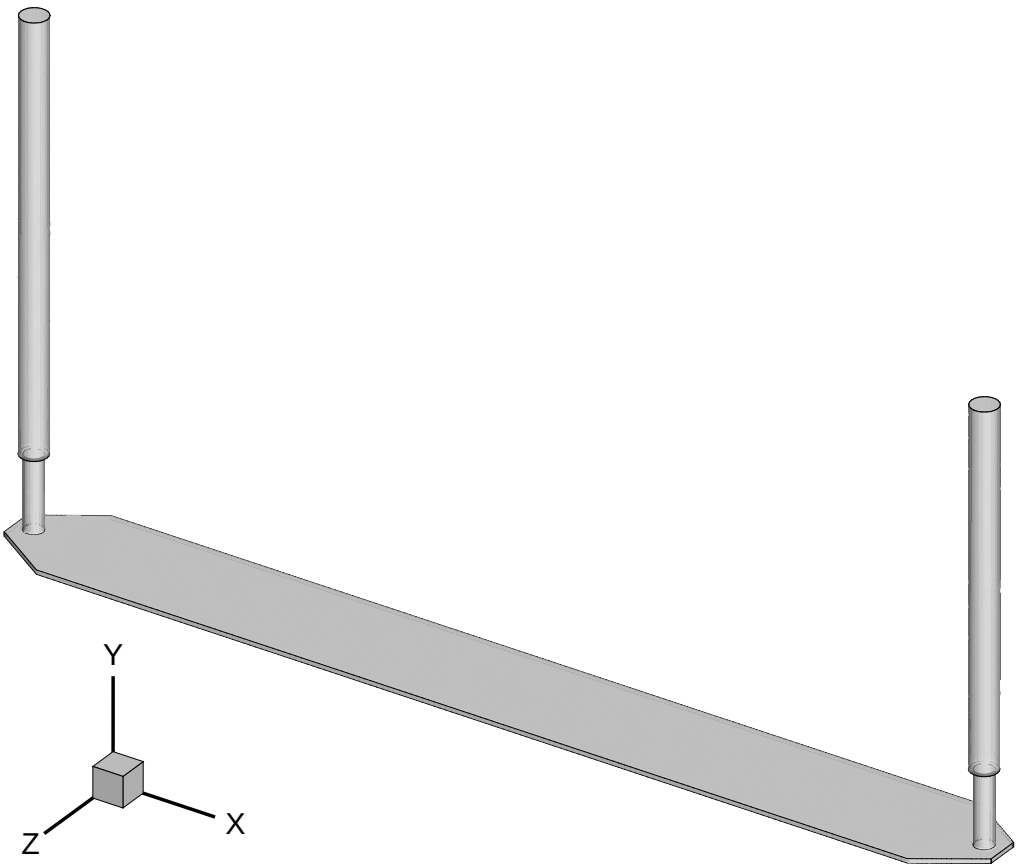

Figure 6.19: Schematic of the flow geometry of the experimental facility.

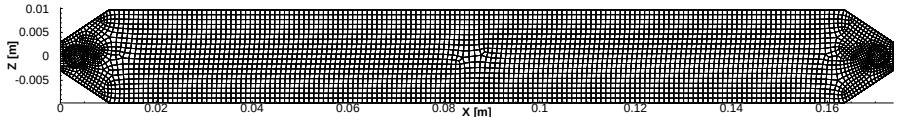

Figure 6.20: Grid used to model the experimental facility.

the acting fluid to eliminate the reactions at the catalyst surface. Pressure drop was measured and modeled at different flow rates. The results of these pressure parametric studies are shown in Figure 6.21. Good agreement is seen between the measured experimental pressure drop and the modeled numerical pressure drop.

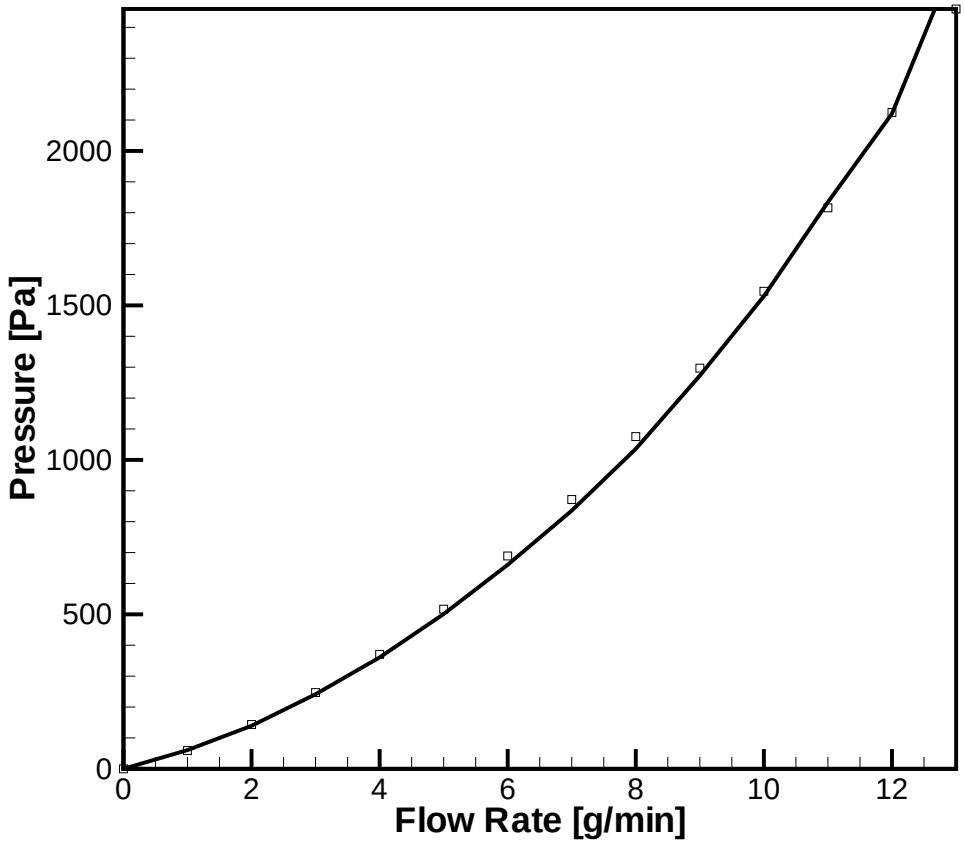

Figure 6.21: Pressure drop through device. The experimental pressure drop is shown with symbols and the numerical pressure drop is given with a solid line.

The geometry used to mesh the grid on which the solution was calculated was

simplified to include only the catalyst section. The catalyst section is seen in Figure 6 where the width of the channel is constant. Assuming no reactions in the gaseous phase allows the bulk mean molar concentrations at the end of the catalyst to be equal to the concentrations at the exit of the device. To capture the velocity of the two geometries, the velocity profiles of both models are compared in Figure 6.22, where the two geometries are under that same mass flow rate. The full mesh allows for more flow through the center of the reactor. The faster peak flow seen in the full mesh will result in shorter residence times and will effect the hydrogen to some degree.

The exit hydrogen concentrations are also studied. The method detailed in Section 6.1 is used to find the bulk mean dry exit concentration of hydrogen by introducing a porous activation constant (first introduced by Wang *et al.* [5]). This activation constant was used through all subsequent simulations. Table 6.5 shows the dry concentration (molar fraction) of hydrogen at the end of the catalyst section. Measuring the dry concentration (the concentration after the steam is removed) was required to analyze the experimental samples. The steam-methane ratio for the samples are given. The temperature found experimentally was enforced at the catalyst wall. (The temperature profile is given in [38].) The temperature enforced for the first four flow rates using Catalyst B is seen in Figure 6.23. The piecewise function of the temperature profile is owing to the seven heated blocks used in the experiment. The percent error is given for five flow rates. The simulated and experimental result agree within 9%.

A porous felt with deposited palladium nanoparticals throughout the felt acted

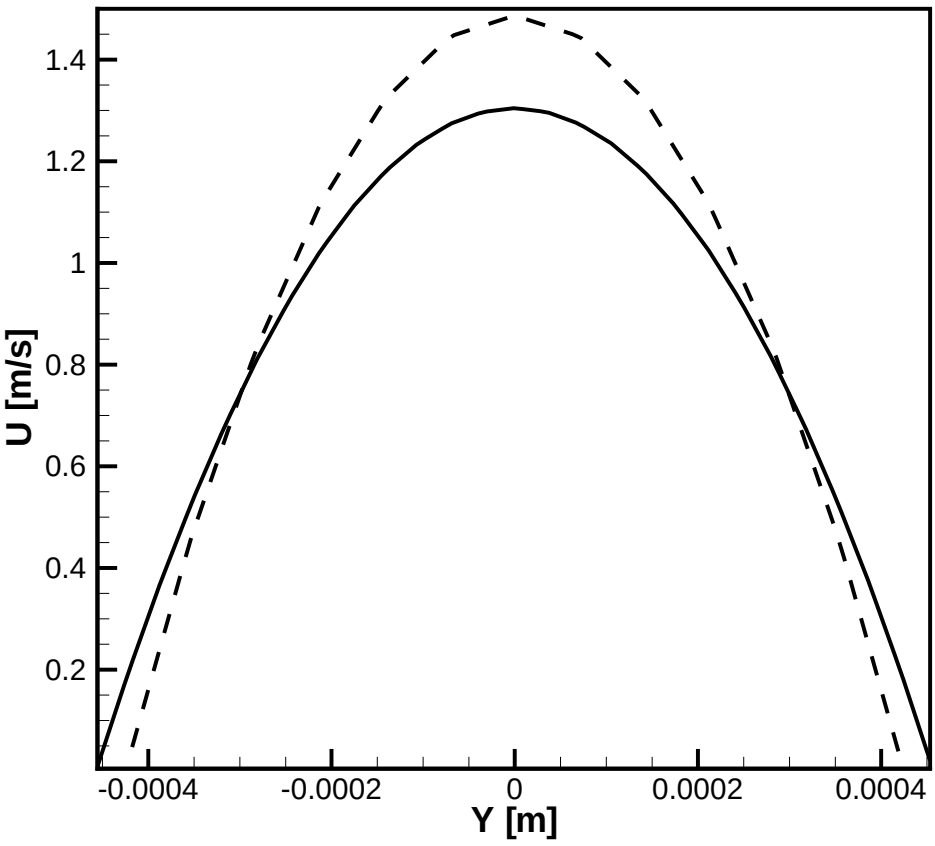

Figure 6.22: Velocity profiles of both the full geometry model and the truncated model. The full model velocity is shown with a dashed line $(--)$ and the truncated model is given with a solid line $(-)$.

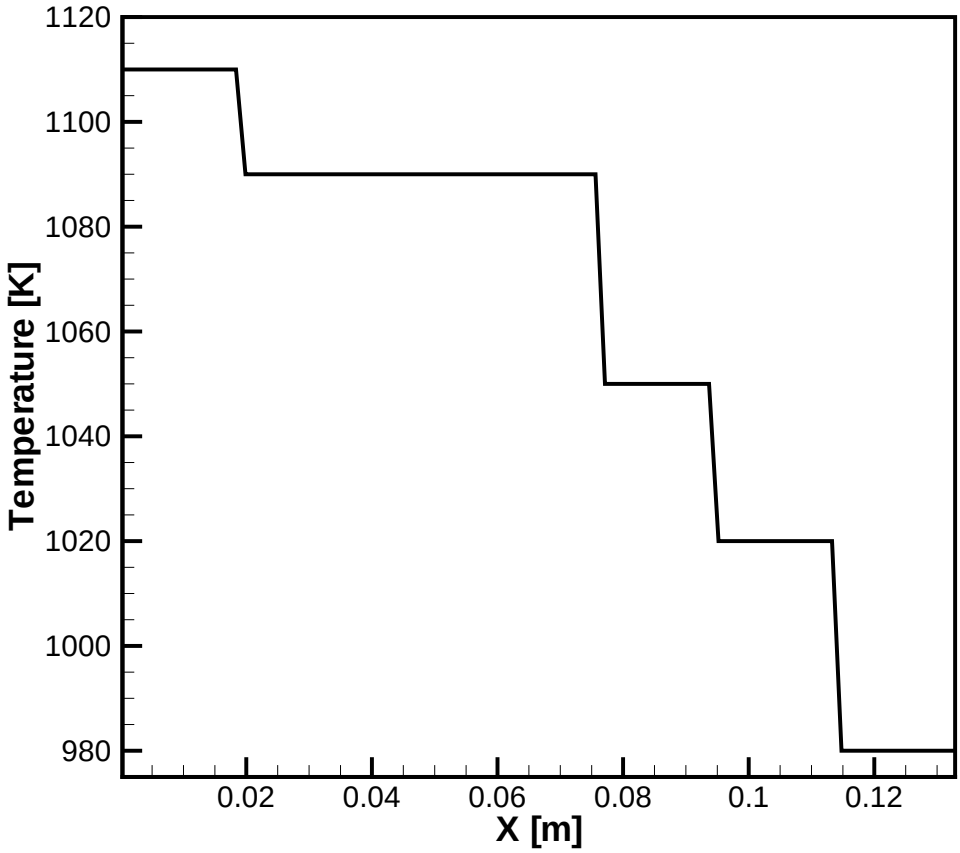

Figure 6.23: Temperature profiles of the first four flow rates using Catalyst B, along the reactor length.

as the catalyst (chemical kinetics characteristics are taken from Shu *et al.* [39]). A number of catalysts were used in this validation study. Detailed descriptions of the different catalysts are given in [38]. For this study it is sufficient to know, "catalyst B" was treated such that the nanoparticles were deposited uniformly throughout the volume of the porous catalyst. The second catalyst sample, "catalyst C", was treated such that the nanoparticles were concentrated near the channel side of the porous volume.

Table 6.5: Hydrogen Production Compared to Experimental Results for Catalyst B

Flow Rate g/min	Steam-Methane Ratio	Eilers H_2 Molar Fraction	Peterson H_2 Molar Fraction	Percent Difference %
0.15	3.27	0.1783	0.1783*	0.000
0.194	3.4	0.1517**	0.1609	6.065
0.194	3.4	0.1532***	0.1524	0.522
0.258	3.4	0.1285	0.1289	0.311
0.388	3.29	0.0969	0.0890	8.152

* Refined case

* Averaged over 2 experimental runs

** Averaged over 3 experimental runs

The same experiment was performed with "catalyst C". The large difference in resulting hydrogen production testifies to the sensitivity of hydrogen production to catalyst characteristics. Table 6.6 shows the experimental and numerical results using "catalyst C". For the experimental data from the "catalyst C" strong velocity dependence was found in resolving the catalyst activation factor C_a, the new model takes the form,

$$C_a = A + Bv, \tag{6.5}$$

where A and B are iteratively found constant and v is the inlet velocity. These A and B constants where found using the data from the fasted and slowest flows from the data set seen in Table 6.6. The expression was then assign to the renaming experiments using "catalyst C". These experiments are ran for a constant wall temperature. The experimental wall temperature for the experiment with a flow rate of 0.149 g/min was a temperature of 1050 K, it was found numerically that these temperatures were achieved with a heat flux of 2.1 kW/m^2. It was found experimentally that less than 10% of the heat added to the system went into the reactor.

Table 6.6: Hydrogen Production Compared to Experimental Results for Catalyst C

Flow Rate g/min	Steam-Methane Ratio	Eilers H_2 Molar Fraction	Peterson H_2 Molar Fraction	Percent Difference %
0.149	2.91	0.4233	0.436	3.01
0.192	2.91	0.3328	0.321	3.54
0.257	3.15	0.2493	0.257	3.10
0.388	3.00	0.1889	0.183	3.11

The chemical species generation and depletion along the channel length can not be measured with the experimental facility utilized in this work, but can be generated from the numerical model. Figures 6.24, 6.25 and 6.26 gives contour plots of hydrogen, methane and velocity. All contour plots are generated for a flow rate 0.149 g/min of methane at the inlet (inlet velocity of 3.0 m/s) and a steam

methane ratio of 2.91 with “catalyst C”.

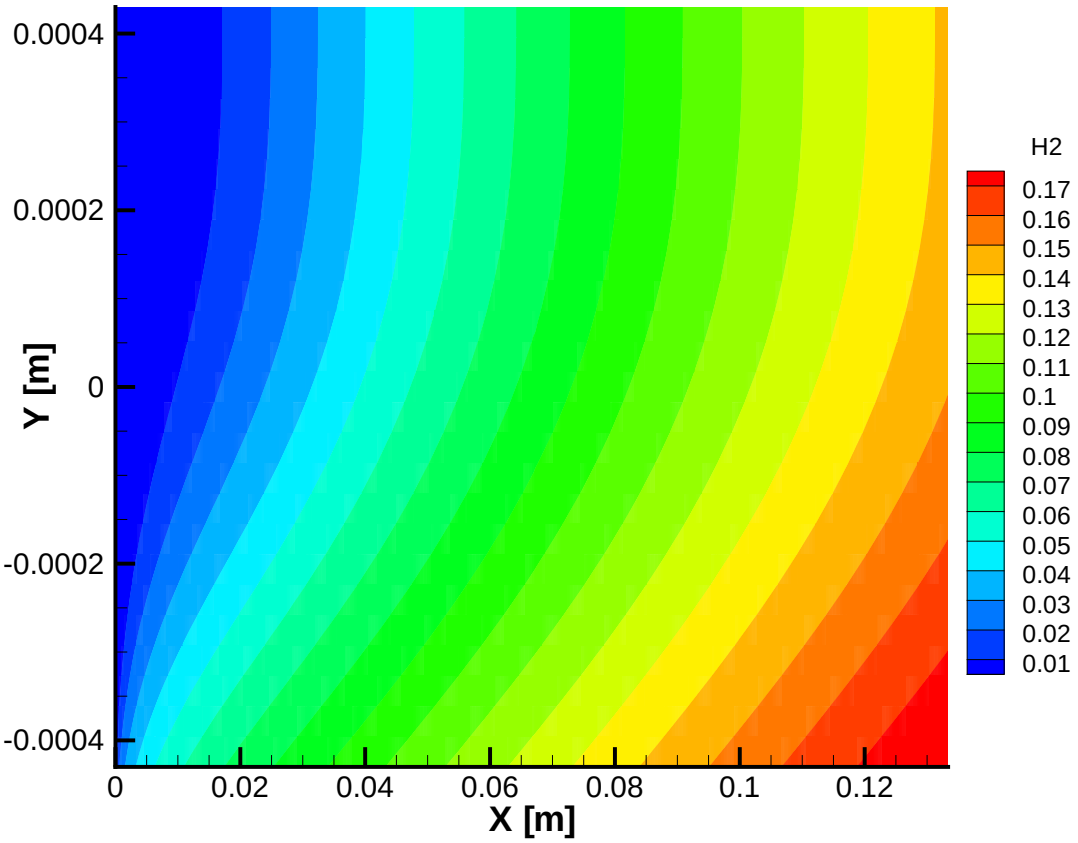

Figure 6.24: Contour of hydrogen molar fraction within the reactor geomentry.

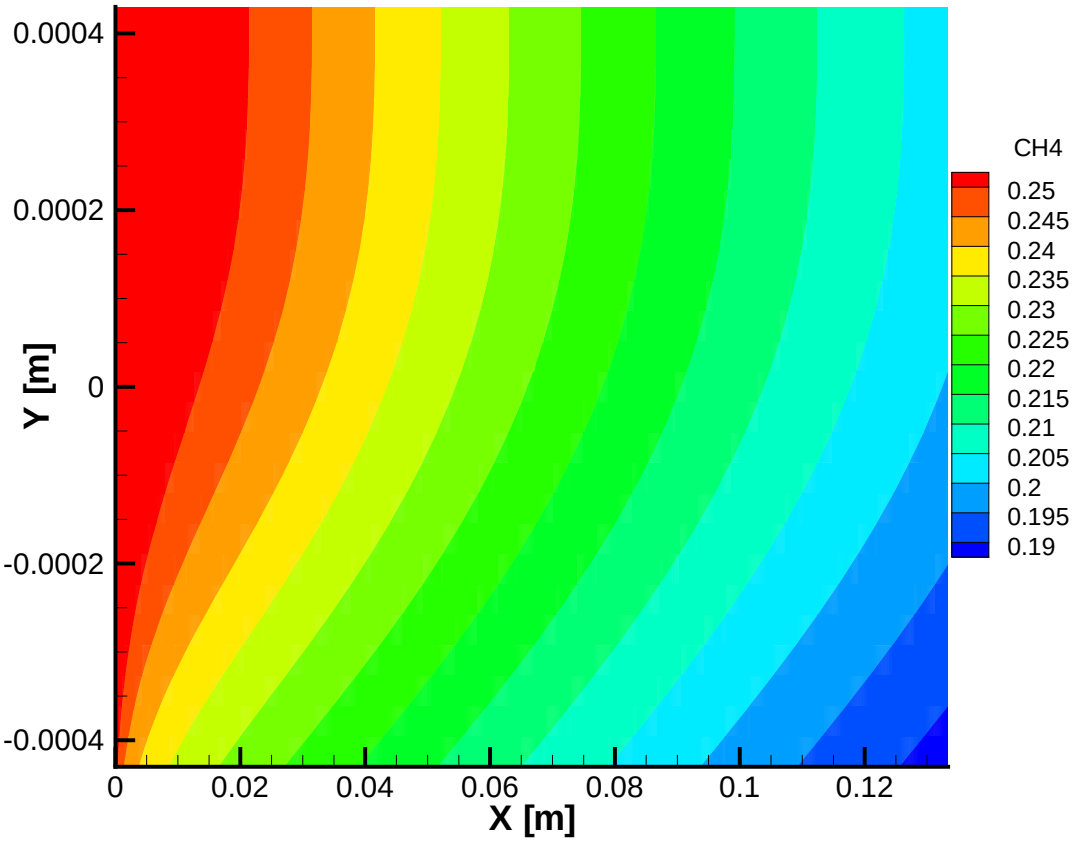

Figure 6.25: Contour of methane molar fraction within the reactor geomentry.

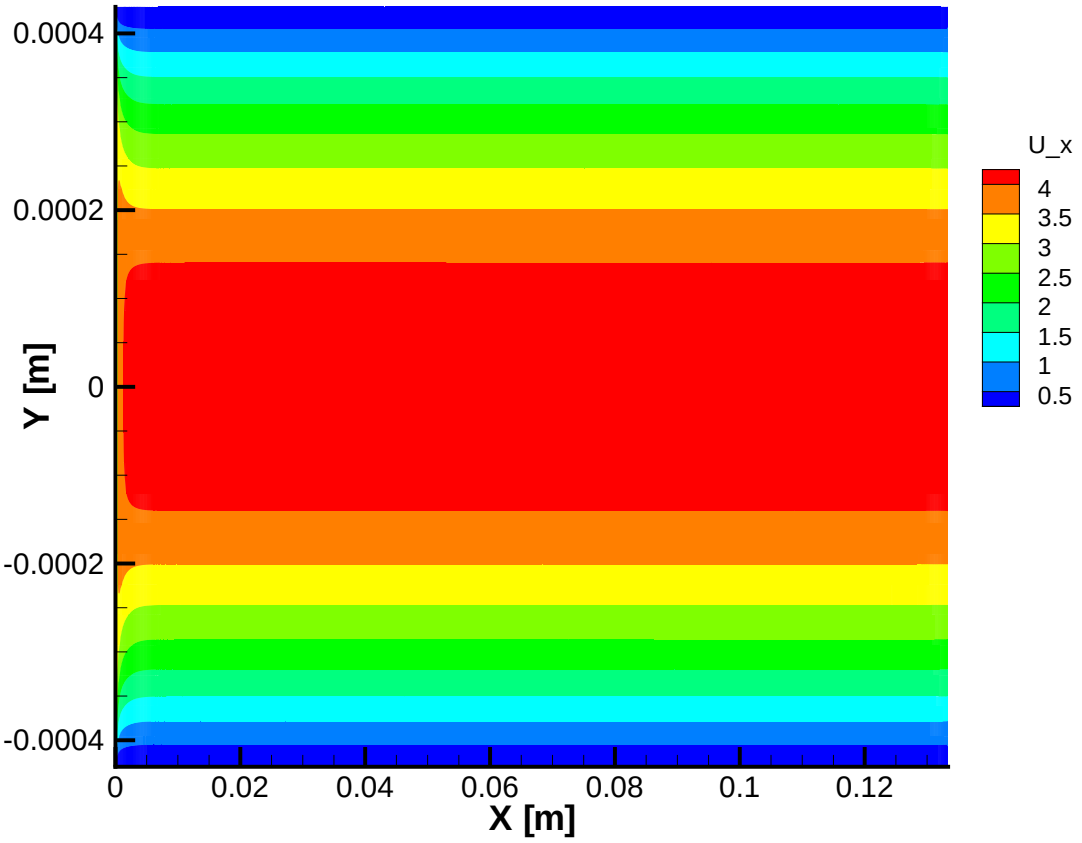

Figure 6.26: Contour of velocity molar fraction within the reactor geomentry.

Chapter 7 – Summary and Conclusions

7.1 Conclusion

Numerical experiments investigating the effectiveness of a micro/mini-channel reactor geometry on methane-steam reforming are performed using a low-Mach number, variable density Navier-Stokes equations together with multicomponent reactions. Methane-steam reforming is modeled by three reduced-order reactions occurring on the reactor walls, two of which are endothermic reactions and one of which is an exothermic water-gas shift reaction. The reaction rate constants are obtained based on the experimental work by Hou and Hughes *et al.* [6] and refined by the work of Wang *et al.* [5]. The predictions of the numerical simulation are first validated against the experimental data for different flow rates to show reasonable agreement of hydrogen production and methane consumption.

The validated numerical model is then applied to perform parametric studies investigating the effect on hydrogen production. The amount of heat flux, the heat flux profile, the steam methane ratio, and the total flow rate were varied. It was found that for all cases the majority of the conversion to hydrogen takes place in the upstream section of the microchannel where the reaction rates are considerably large. With the production of products such as carbon monoxide, carbon dioxide, and hydrogen, the reaction rates drop along the length of the channel. It was found that manipulating the wall heat flux profile can result in optimal hydrogen production for a specific steam methane ratio. It was also found that accurate quantification of the reaction rates and porosity of the catalyst surface are critical for numerical model predictions.

The results of the parametric study allows for the evaluation of system performance. The heat flux magnitude is directly correlated with increased heat flux (temperature) with increased hydrogen production. Materials limit the high temperature attainable from reactor devices. Hydrogen production of 10% (mole fraction) was observed when increasing the heat flux from no additional heat flux to a wall heat flux of 3 kW/m^2. The reaction rate sensitivity to temperature explains the higher production rates hydrogen for high temperatures.

The results of the heat flux profile study is increased hydrogen production with a ramp up heat flux, where the heat flux varies linearly from zero at the start of the catalyst section to twice the average heat flux at the end of the catalyst. The ramp up profile performed better than the uniform heat flux profile and the ramp down profile (where heat flux varies lineally with a maximum at the start of the catalyst). While the ramp up profile produced the most hydrogen, the increase of hydrogen production between the ramp down profile (worst performer) and the ramp up profile was only 3.5%. The better behavior of the ramp up case is explained by increasing the average reaction rates along the reactor length. Near the start of the catalyst the high mole fraction of methane and steam drive the reaction rates up. In addition, the high temperature for the ramp up profile drives the reaction rates near the end of the catalyst. Kuznetsov *et al.* [40] found for a reactor of 225 height lengths that the ramp down profile performed better than the uniform profile. (The ramp up profile was not studied). This finding is consistent with this work which has a reactor length of only 29 height lengths. A longer reactor geometry will allow for more complete combustion, after which heating near the

end of the catalyst only heats the exit gases, and does not promote reactions.

Hydrogen production is inversely correlated with flow rate; slower flow rates allow for longer resident time for the reactants in the reactor. Varying flow rates from 800 ml/min to 100 ml/min results in an increase of hydrogen mole fraction of 16%. The increase in hydrogen mole fraction comes at the cost of lower through put. To optimize the flow rate, a cost-benefit measurement must be introduced to weigh increased hydrogen production against decreased through put.

The steam methane reaction has a nonlinear effect on hydrogen production. A maximum production of hydrogen is observed near a steam ratio of 3.0, with a notable drop off of hydrogen production both above and below this ratio. The full range of ratios studied here has a large effect on hydrogen production. Hydrogen production varied 20% (molar basis) for a range of steam methane ratio between 1 and 4. This wide range of hydrogen production rates is seen chiefly in the poor performance of the ratio of 1, where 16.5% of the improved performance is observed between the ratios of 1 and 2. There is little change in performance when the steam methane ratio is between 2 and 4 (approximately 4.0%).

APPENDICES

A-1 Fluid Properties

The fluid properties are taken from a variety of different sources. The properties are allowed to vary with both temperature and chemical species. Assuming low Mach number allows the properties changes with pressure to be neglected. Owing to the small changes in specific heat (C_p) and the difficulty of handling varying specific heat it is held constant for all temperatures and allowed to vary only with chemical species. The diffusion coefficient ($\mathcal{D}_i$), was assumed to vary only with temperature, which is consistent with the work by Kuznetsov & Kozlov [4].

The molecular weight (M_i) and enthalpy of formation ($h^0_{f_i}$) for all species are taken from **Fundamentals of engineering thermodynamic** [32], which are recorded below. The viscosity (μ) and specific heat (C_p) are taken from **Physical properties: a guide to the physical, thermodynamic, and transport property data of industrially important chemical compounds** [31].

Table 1: Molecular Weight, Enthalpy of Formation and Specific Heat for all Species

Species	Molecular Weight (M_i)	Enthalpy of Formation ($h^0_{f_i}$)	Specific Heat (C_p)
	$kg/kmol$	$kJ/kmol$	$kJ/kg-K$
CH_4	16.0	-9.0×10^4	4.46
H_2O	18.0	-2.48×10^5	2.3
H_2	2.01	0.0	15.0
CO	28.0	-1.12×10^5	1.18
CO_2	44.0	-3.95×10^5	1.23

The viscosity of each species is given in the following expressions, where T is the temperature in kelvin and the units of μ_i are $[N-s/m^2]$, the given equations are modified from [31] to express the properties into appropriate units. Figure 1

captures these properties over the temperature range investigated here.

$$\mu_{CH_4} = 1.596 \times 10^{-7} + 3.439 \times 10^{-9}T - 8.140 \times 10^{-13}T^2 \quad (1)$$

$$\mu_{H_2O} = -3.189 \times 10^{-7} + 4.145 \times 10^{-9}T - 8.272 \times 10^{-14}T^2 \quad (2)$$

$$\mu_{H_2} = 2.187 \times 10^{-7} + 2.22 \times 10^{-9}T - 3.75 \times 10^{-13}T^2 \quad (3)$$

$$\mu_{CO} = 3.228 \times 10^{-7} + 4.747 \times 10^{-9}T - 9.648 \times 10^{-13}T^2 \quad (4)$$

$$\mu_{CO_2} = 2.545 \times 10^{-7} + 4.549 \times 10^{-9}T - 8.649 \times 10^{-13}T^2 \quad (5)$$

The diffusion coefficient is taken from Kuznetsov *et al.* [4], where the units of $\mathcal{D}_i$ are $[m^2/s]$. Here the operating pressure as atmospheric or 101 kPa and assumed constant.

$$\mathcal{D}_i = 9.99 \times 10^{-10}T^{1.75} \quad (6)$$

The mixture viscosity model is taken from **Transport Phenomena** [41] based on the work of Buddenberg *et al.* [42]. All other mixture properties are taken as the mass fraction weighted average, seen previously.

$$\mu_{mix} = \sum_{i=1}^{ns} \frac{x_i \mu_i}{\sum_{j=1}^{ns} x_j \Phi_{ij}}, \quad (7)$$

where,

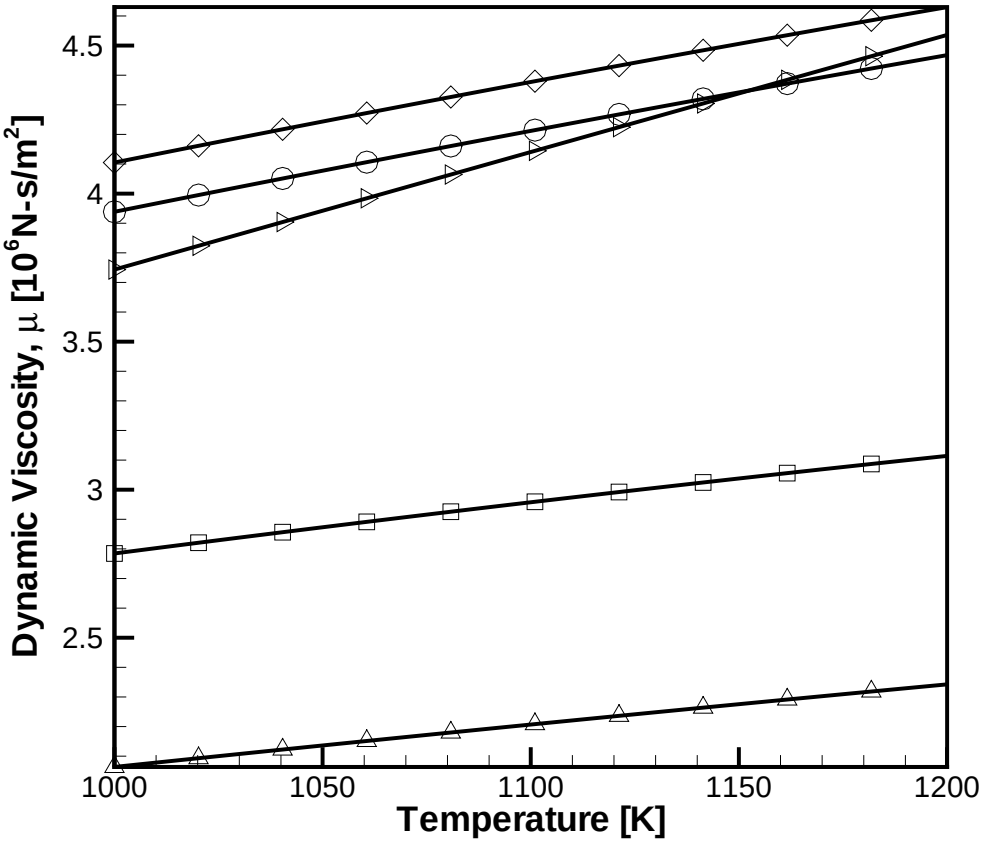

Figure 1: Fluid dynamic viscosity of all species investigated over a temperature range of 1000 K to 1200 K.

$$\Phi_{ij} = \frac{1}{\sqrt{8}} \left(1 + \frac{M_i}{M_j}\right)^{-1/2} \left(1 + \left(\frac{\mu_i}{\mu_j}\right)^{1/2} + \left(\frac{M_i}{M_j}\right)^{1/2}\right)^2, \tag{8}$$

where ns is the number of chemical species and x_i and x_j are the mole fractions of the i^{th} and j^{th} species.

A-2 Grid Refinement

The grid resolution will be considered in this section. Three grids are generated for grid tests. Grid one has 25 control volumes (CVs) in the cross flow direction, Grid two has 36 CVs in the cross flow direction and Grid three has 50 CVs in the cross flow direction. All three grids are formed using a uniform Cartesian mesh geometry. These tests are preformed on the parametric studies geomentry, see in Figure 2.

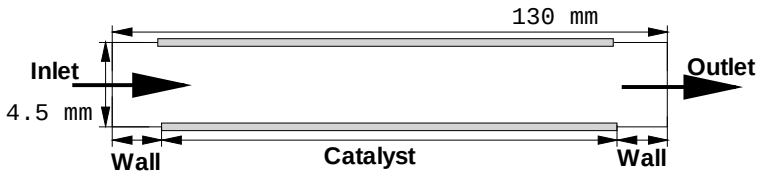

Figure 2: Schematic of the microchannel reactor used for the grid refinement studies.

To show the agreement (or disagreement) between the three grids two flow characteristics are investigated; 1) x-direction velocity and 2) mole fraction. Both plots below are taken at a flow length of 100 mm. Figure 3a shows the velocity field for all three grids and Figure 3b shows the mole fraction of hydrogen in the cross flow direction.

All three grid give solution fields within 0.24% of eachother. Therefore, the least refined grid gives a grid independent solution which is the grid geometry used in this study.

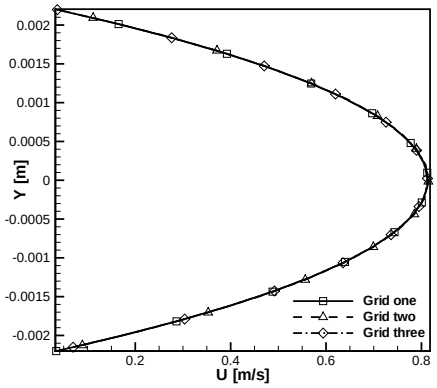

(a)

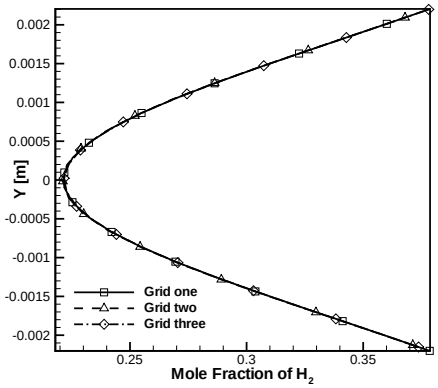

(b)

Figure 3: Velocity profiles (a) and mole fraction profiles of hydrogen (b) at a flow length of 100 mm in the cross flow direction for three grid geometries. Where Grid one has 25 CVs in the cross flow direction, Grid two has 36 CVs and grid three has 50 CVs

Bibliography

[1] Qu, W. and Mudawar, I., 2002, "Experimental and numerical study of pressure drop and heat transfer in a single-phase micro-channel heat sink," International Journal of Heat and Mass Transfer, **45**(12), pp. 2549–2565.

[2] Kakaç, S., Shah, R., and Aung, W., 1987, *Handbook of single-phase convective heat transfer*, Wiley New York et al.

[3] Mills, A., 2001, *Mass transfer*, Prentice Hall Upper Saddle River, NJ.

[4] Kuznetsov, V. and Kozlov, S., 2008, "Modeling of methane steam reforming in a microchannel with a heat flow distributed in length," Journal of Engineering Thermophysics, **17**(1), pp. 53–59.

[5] Wang, Y., Yoshiba, F., Kawase, M., and Watanabe, T., 2009, "Performance and effective kinetic models of methane steam reforming over Ni/YSZ anode of planar SOFC," International Journal of Hydrogen Energy.

[6] Hou, K. and Hughes, R., 2001, "The kinetics of methane steam reforming over a Ni/α-Al2O catalyst," Chemical Engineering Journal, **82**(1-3), pp. 311–328.

[7] Deutschmann, O. and Schmidt, L., 1998, "Modeling the partial oxidation of methane in a short-contact-time reactor," AIChE Journal, **44**(11), pp. 2465–2477.

[8] Tamme, R., Buck, R., Epstein, M., Fisher, U., and Sugarmen, C., 2001, "Solar upgrading of fuels for generation of electricity," Journal of Solar Energy Engineering, **123**, p. 160.

[9] Möller, S., Kaucic, D., and Sattler, C., 2006, "Hydrogen production by solar reforming of natural gas: a comparison study of two possible process configurations," Journal of Solar Energy Engineering, **128**, p. 16.

[10] Kodama, T., Moriyama, T., Shimoyama, T., Gokon, N., Andou, H., and Satou, N., 2006, "Ru/ Ni–Mg–O catalyzed SiC-foam absorber for solar reforming receiver-reactor," Journal of Solar Energy Engineering, **128**, p. 318.

[11] Wegeng, R., TeGrotenhuis, W., and Mankins, J., 2007, "Solar thermochemical production of fuels," AIAA, 2007-4709, 5th International Energy Conversion Engineering Conference and Exhibit.

[12] Li, G., Shrotriya, V., Huang, J., Yao, Y., Moriarty, T., Emery, K., and Yang, Y., 2005, "High-efficiency solution processable polymer photovoltaic cells by self-organization of polymer blends," Nature Materials, **4**(11), pp. 864–868.

[13] Yu, G., Gao, J., Hummelen, J., Wudl, F., and Heeger, A., 1995, "Polymer photovoltaic cells: enhanced efficiencies via a network of internal donor-acceptor heterojunctions," Science, **270**(5243), p. 1789.

[14] Hagfeldt, A. and Gratzel, M., 2000, "Molecular photovoltaics," Acc. Chem. Res, **33**(5), pp. 269–277.

[15] Tanaka, S., Chang, K., Min, K., Satoh, D., Yoshida, K., and Esashi, M., 2004, "MEMS-based components of a miniature fuel cell/fuel reformer system," Chemical Engineering Journal, **101**(1-3), pp. 143–149.

[16] Wang, X. and Gorte, R., 2001, "Steam reforming of n-butane on Pd/ceria," Catalysis Letters, **73**(1), pp. 15–19.

[17] Moon, D., Sreekumar, K., Lee, S., Lee, B., and Kim, H., 2001, "Studies on gasoline fuel processor system for fuel-cell powered vehicles application," Applied Catalysis A: General, **215**(1-2), pp. 1–9.

[18] Roychoudhury, S., Castaldi, M., Lyubovsky, M., LaPierre, R., and Ahmed, S., 2005, "Microlith catalytic reactors for reforming iso-octane-based fuels into hydrogen," Journal of Power Sources, **152**, pp. 75–86.

[19] Wegeng, R. and Mankins, J., 2009, "Space power systems: Producing transportation (and other chemical) fuels as an alternative to electricity generation," Acta Astronautica, **65**(9-10), pp. 1261–1271.

[20] Steinfeld, A., 2005, "Solar thermochemical production of hydrogen—-a review," Solar Energy, **78**(5), pp. 603–615.

[21] Röger, M., Pfander, M., and Buck, R., 2006, "Multiple air-jet window cooling for high-temperature pressurized volumetric receivers: Testing, evaluation, and modeling," Journal of Solar Energy Engineering, **128**(3), pp. 265–274.

[22] Kraupl, S. and Steinfeld, A., 2001, "Pulsed gas feeding for stoichiometric operation of a gas-solid vortex flow solar chemical reactor," Journal of Solar Energy Engineering, **123**, p. 133.

[23] Xu, J. and Froment, G., 1989, "Methane steam reforming, methanation and water-gas shift: I. Intrinsic kinetics," AIChE Journal, **35**(1), pp. 88–103.

[24] Appel, C., Mantzaras, J., Schaeren, R., Bombach, R., Inauen, A., Tylli, N., Wolf, M., Griffin, T., Winkler, D., and Carroni, R., 2005, "Partial catalytic oxidation of methane to synthesis gas over rhodium: in situ raman experiments and detailed simulations," Proceedings of the Combustion Institute, **30**(2), pp. 2509 – 2517.

[25] Levent, M., J. Gunn, D., and Ali El-Bousiffi, M., 2003, "Production of hydrogen-rich gases from steam reforming of methane in an automatic catalytic microreactor," International Journal of Hydrogen Energy, **28**(9), pp. 945–959.

[26] Kenneth, K., 2005, "Principles of combustion," John Wiley's sons, Ine, Hoboken, New Jersey.

[27] Turns, S., 1995, "An introduction to combustion: Concepts and applications(Book)," New York: McGraw-Hill, Inc, 1995.

[28] Versteeg, H. and Malalasekera, W., 1995, "An Introduction to CFD. The Finite Volume Method," .

[29] Kakaç, S. and Yener, Y., 1995, *Convective heat transfer*, CRC.

[30] Pierce, C. and Moin, P., 2004, "Progress-variable approach for large-eddy simulation of non-premixed turbulent combustion," Journal of Fluid Mechanics, **504**, pp. 73–97.

[31] Yaws, C., 1977, "Physical properties: a guide to the physical, thermodynamic and transport property data of industri," .

[32] Moran, M. and Shapiro, H., 2003, *Fundamentals of engineering thermodynamics*, John Wiley & Sons New York.

[33] Froment, G., Bischoff, K., and Froment, G., 1990, "Chemical reactor analysis and design," .

[34] Stutz, M. J. and Poulikakos, D., 2005, "Effects of microreactor wall heat conduction on the reforming process of methane," Chemical Engineering Science, **60**(24), pp. 6983 – 6997.

[35] Martin, M., Patton, C., Schmitt, J., and Apte, S., 2009, "Direct Simulation Based Model-Predictive Control of Flow Maldistribution in Parallel Microchannels," Journal of Fluids Engineering, **131**, p. 111201.

[36] Incropera, F., DeWitt, D., Bergman, T., and Lavine, A., 1996, *Fundamentals of heat and mass transfer*, John Wiley & Sons New York.

[37] Munson, B., Young, D., Okiishi, T., and Young, D., 1998, *Fundamentals of fluid mechanics*, Wiley New York etc.

[38] Eilers, B., 2010, *Steam Methane Reforming Under Constant and Variable Surface Temperature Distributions*, Master's thesis, Oregon State University, Corvallis, Oregon.

[39] Shu, J., Grandjean, B., and Kaliaguine, S., 1994, "Methane steam reforming in asymmetric Pd-and Pd-Ag/porous SS membrane reactors," Applied Catalysis A: General, **119**(2), pp. 305–325.

[40] Kuznetsov, V., Vitovsky, O., and Gasenko, O., 2009, "Methane steam reforming in an annular microchannel with Rh/Al_2O_3 catalyst," Journal of Engineering Thermophysics, **18**(3), pp. 187–196.

[41] Bird, R., Stewart, W., and Lightfoot, E., "Transport Phenomena, Wiley, New York, 1960," .

[42] Buddenberg, J. and Wilke, C., 1949, "Calculation of Gas Mixture Viscosities." Industrial & Engineering Chemistry, **41**(7), pp. 1345–1347.